8-2010

Study of Deformation Behavior of Nanocrystalline Nickel using Nanoindentation Techniques

Changli Wang
cwang17@utk.edu

To the Graduate Council:

I am submitting herewith a dissertation written by Changli Wang entitled "Study of Deformation Behavior of Nanocrystalline Nickel using Nanoindentation Techniques." I have examined the final electronic copy of this dissertation for form and content and recommend that it be accepted in partial fulfillment of the requirements for the degree of Doctor of Philosophy, with a major in Materials Science and Engineering.

T. G. Nieh, Major Professor

We have read this dissertation and recommend its acceptance:

E. P. George, P. K. Liaw, S. Q. Wang

Accepted for the Council:
Dixie L. Thompson

Vice Provost and Dean of the Graduate School

(Original signatures are on file with official student records.)

To the Graduate Council:

I am submitting herewith a dissertation written by Changli Wang entitled "Study of Deformation Behavior of Nanocrystalline Nickel using Nanoindentation Techniques." I have examined the final electronic copy of this dissertation for form and content and recommend that it be accepted in partial fulfillment of the requirements for the degree of Doctor of Philosophy, with a major in Materials Science and Engineering.

T. G. Nieh, Major Professor

We have read this dissertation
and recommend its acceptance:

E. P. George

P. K. Liaw

S. Q. Wang

Accepted for the Council:

Carolyn R. Hodges

Vice Provost and Dean of the Graduate School

(Original signatures are on file with official student records.)

Study of Deformation Behavior of Nanocrystalline Nickel using Nanoindentation Techniques

A Dissertation Presented for the

Doctoral Philosophy Degree

The University of Tennessee, Knoxville

Changli Wang

August 2010

Dedication

This dissertation is lovingly dedicated to my parents, Yinshan Wang and Shumei Lin, for their unconditional love and support.

Acknowledgement

I would like to thank my advisor Prof. T. G. Nieh, who I am so grateful to be able to study under his guidance, for given me this opportunity and his patience, encouragement over years. He has acted as an advisor and mentor throughout the entire of my work. I will always consider him my greatest teacher for it is from him that I have not only learned a great deal of materials science, but also the way to be a materials scientist. I also would like to thank the other members of my committee, Prof. E. P. George, Prof. P. K. Liaw and Prof. S. Q. Wang for your insightful critique and advice.

There are many people to whom I owe a debt of gratitude for completing my Doctor of Philosophy Degree in Materials Science and Engineering. First, Dr. Y. H. Lai and H. S. Chou, who prepared micro pillar samples, which make studying of uniaxial compression behavior of thin films possible, Dr. M. Zhang whose work on TEM study and thoughts was sincerely appreciated. I am grateful to the faculty and staff in the Materials Science and Engineering Department at the University of Tennessee and my group members Dr. S. X. Song, X. X. Sheng, L. Wang, C. Zhu for their help and friendship. I would like to give my special gratitude to my best friends S. J. Xie and D. C. Qiao whose friendship made my studying life joyful. Finally, I would like to thank my sister C. W. Wang, my brother C. B. Wang, A. G. Liu and Tony for their love and support over the years.

Financial support for this work from the Division of Materials Science and Engineering, Office of Basic Energy Sciences, U. S. Department of Energy under contact DE-FG02-06ER46338 with the University of Tennessee is gratefully acknowledged.

Instrumentation for the nanoindentation work was jointly funded by the Tennessee Agriculture Experiment Station and UT College of Engineering.

Abstract

Nanocrystalline materials with grain size less than 100 nm have been receiving much attention because of their unparallel properties compared with their microcrystalline counterparts. Because of its high hardness, nanocrystalline nickel has been used for MEMS. Long term thermomechnical properties and deformation mechanism at both ambient and elevated temperatures need to be evaluated which is vital for reliability of its applications as structural material.

In this thesis, nanoindentation creep of nanocrystalline nickel with an as-deposited grain size of 14 nm was characterized at elevated temperatures. The nanoindentation creep rate was observed to scale with temperature and applied load (or stress), and could be expressed by an empirical power-law equation for describing conventional crystalline solids. Creep activation energy was found to be close to that for grain boundary self-diffusion in nickel. The activation volume was also evaluated using a stress relaxation technique. The creep results were compared with those for fine-grained nickel in the literature. Possible mechanisms were discussed in light of the creep rate and temperature ranges.

To provide a direct comparison, uniaxial creep tests were conducted on nanocrystalline nickel with an as-deposited grain size of 14 nm at 398 K. It was found that stress exponents under the two test conditions are almost the same, indicating a similar creep mechanism. However, the strain rate measured by nanoindentation creep was about 100 times faster than that by uniaxial creep. The rate difference was discussed in terms of stress states and the appropriate selection of Tabor factor.

To further explore the time-dependent plastic behavior, multiple unload-reload tests were conducted on electrodeposited nanocrystalline nickel in both compression and tension. A hysteresis was observed during each unload-reload cycle, indicating irreversible energy dissipation. The dissipated energy was evaluated and the energy dissipation rate was found to increase with the flow stress to the third power and sensitive to the stress state (tension or compression). A mechanistic model based on grain boundary sliding was proposed to describe the unload-reload behavior. Experimental results were found to be in good agreement with the model predictions, suggesting the observed hysteresis was indeed caused by grain boundary sliding.

Table of Contents

List of Tables

List of Figures

Chapter 1 Introduction

Nanocrystalline (nc) materials have been studied extensively during the past two decades. Long-term thermomechanical properties for the application of nc materials in MEMS devices need to be addressed. Conventional techniques are not applicable for extracting properties of samples with a limited volume. Nanoindentation is a viable and practical technique for evaluating the deformation behavior of such small devices. However, in order to make full use of the data from nanoindentation creep and make a fair comparison between the data obtained from nanoindentation creep and that from conventional creep, it is necessary to ascertain the correlation between indentation creep rate and uniaxial creep rate. The deformation behavior of nc-materials strongly depends on grain size and grain boundary structure. The reduced grain size promotes grain boundary processes become dominant deformation mechanism. However, it is hard to obtain direct evidence of grain boundary sliding since the impossibility to put inert mark on a nc-sample. An indirect way to evaluate the role of grain boundary sliding in the deformation of nc-material at ambient temperature is by conducting multiple unload-reload tests, i.e. cyclic loading. Amongst many possible mechanisms for mechanical hysteresis available in the coarse-grained counterparts, grain boundary sliding and relaxation believed to contribute to the mechanical hysteresis in nc-materials.

A direct comparison between data from nanoindentation creep and uniaxial creep is limited, especially at elevated temperature, which make this study is of interest. To my best knowledge, conducting cyclic loading on micro-sized samples to study grain boundary sliding related mechanical hysteresis of nc-materials is also new. The purpose of the

current study is to gain a better understanding on the creep behavior of nc-materials at elevated temperatures and to investigate the role of grain boundary sliding during mechanical hysteresis of nc-materials.

1.1 Nanocrystalline Materials

Nanocrystalline materials are defined as materials with grain size is less than 100 nm, which have been the subject of widespread research in the past two decades since the landmark paper by Gleiter [1]. The development of nc-materials has been documented in many reviews [1-15]. The ever increasing interest and efforts in nc-materials is due to unusual properties over their microcounterparts. These unusual properties are invariantly related to the microstructure of the materials. A two-dimensional model of nc material is shown in Figure 1.1 [1]. The grain boundary atoms are white, while the intragranular atoms are in black.

The high volume fraction of grain boundaries inside the materials serves as an effective barrier for the motion of dislocations and the strength follows the traditional Hall-Petch relationship. The grain size dependence of the volume fraction of grain boundaries is shown in Figure 1.2 [16]. The volume fraction of intercrystals and triple junctions is also included in the Figure. Generally, the volume fraction of grain boundaries, intercrystals and triple junctions increases as grain size decreases. However, as the grain size decreases to below some critical value, further decreases grain size, the volume fraction of grain boundaries decreases at which an inverse Hall-Petch relationship will be observed. The number of dislocations piling up against grain boundaries decreases significantly with grain size as shown schematically in Figure 1.3 [17]. This indicates that

strength cann't increases infinitely with decreasing grain size. At some critical value d_c, strength reaches it maximum. Grain size dependence of strength or hardness is schematically shown in Figure 1.4 [18]. The critical value d_c marks the transition from intragranular controlled deformation process to intergranular one i.e. grain boundary dominated process. Not only the strength is directly related to the volume fraction of grain boundary but also deformation process such as time dependent plasticity, i.e. creep, which is important for the application of nc- materials in the field requiring long-term stability such as MEMS devices [19-20].

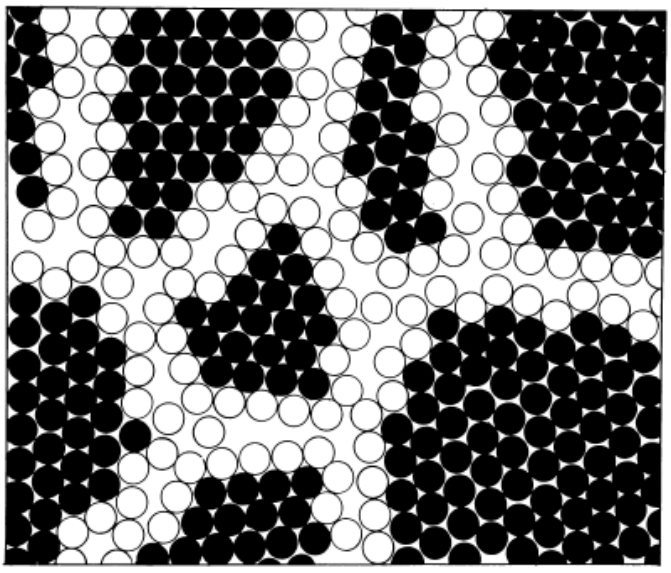

Figure 1.1 Atomic structure of two-dimensional nanostructured materials. The atoms in the centers of the crystals are indicated in black. The ones in the boundary core regions are represented as open circles [1].

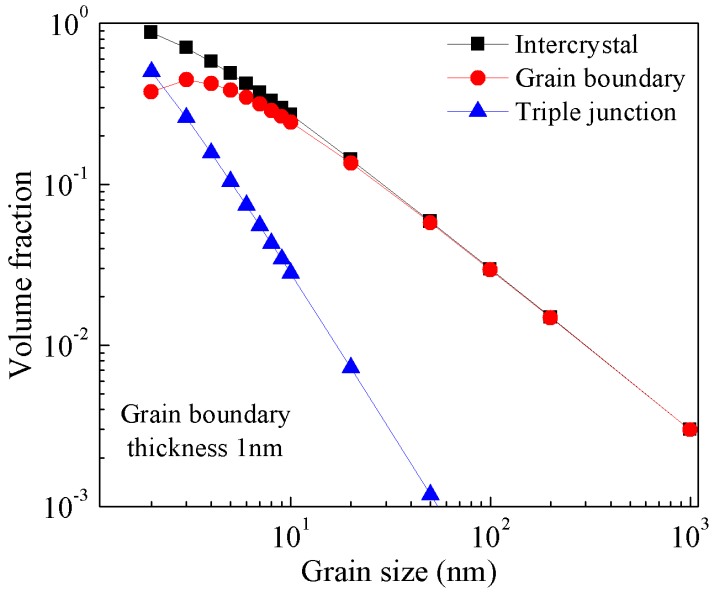

Figure 1.2 Effect of grain size on the volume fraction of intercrystals, grain boundaries and triple junctions [16].

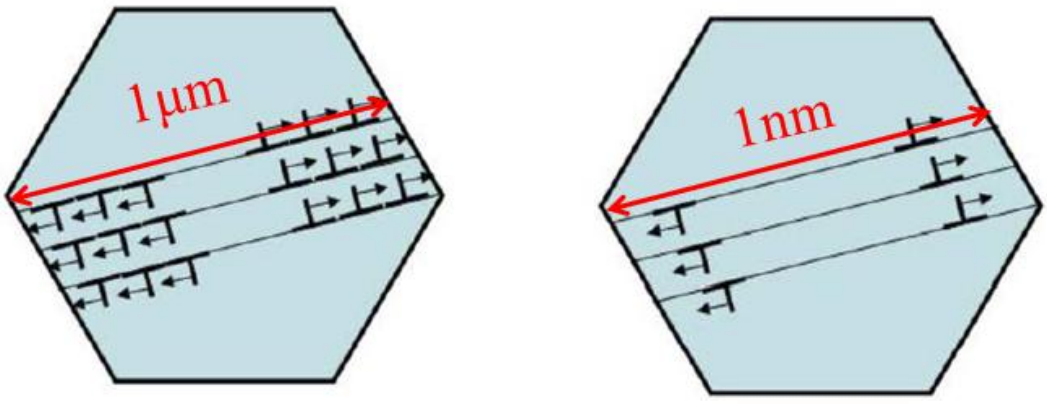

Figure 1.3 Schematic configuration of dislocation pile up in (a) polycrystalline material and (b) nanocrystalline material [17].

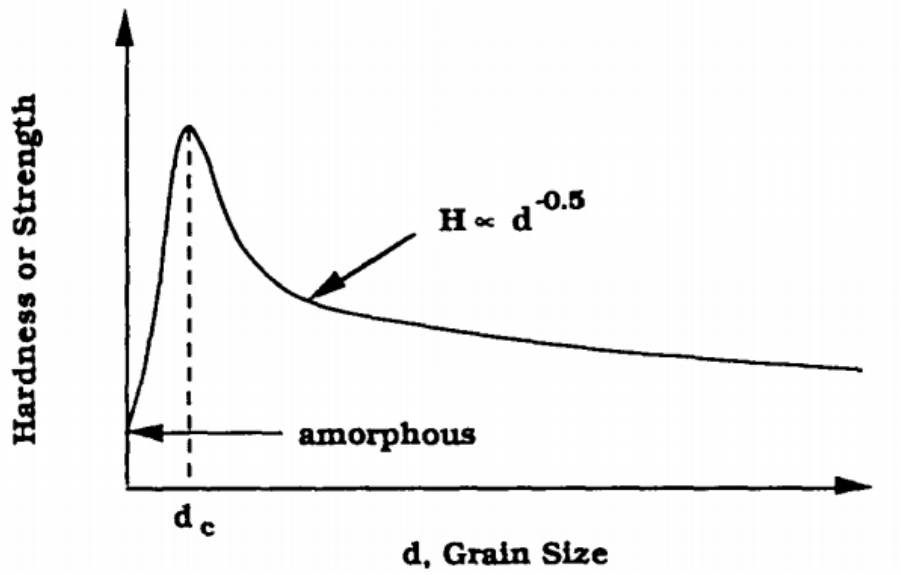

Figure 1.4 Schematic diagram showing grain size dependence of strength or hardness [18].

1.2 Time Dependent Plasticity – Creep

Over the past century, creep of microcrystalline (mc), i.e. coarse-grained, materials has been widely studied and the models are well developed to describe the deformation features and explain the atomic mechanisms. The general equation used to relate creep rate $\dot{\varepsilon}$, stress σ and temperature T is the empirical power-law creep equation [21]:

$$\dot{\varepsilon} = A\sigma^n \exp(-Q/RT) \tag{1-1}$$

where A is a structure-dependent constant, Q is activation energy, R is the gas constant and n is the stress exponent, an indicator of creep mechanism. The expanded forms of equation (1-1) for different creep mechanisms are listed in Table 1.1 [22]. Where D_l and

D_{gb} are the coefficients of lattice and grain boundary diffusion, respectively. G is shear modulus, b is Burgers vector, Ω is atomic volume, δ is the grain boundary thickness and k is Boltzmann's constant. The other parameters are specified in equation (1-1). The grain size d and stress exponent n dependence of creep mechanism can be readily seen in Table 1.1. These constitutive equations have been extended its application in mc-materials to analyze creep results for nc-materials.

1.2.1 Uniaxial Creep of nc Materials

Comparing to the widely investigation on the creep of mc-materials, study of creep in nc-materials is relatively short due to several complications. First, the limitation of processing technique can not produce bulk nc-materials free of defects (porosity, flaws or impurities) with uniform grain size distribution that could represent the material's intrinsic properties. The high volume fraction of grain boundaries, triple junctions and quadruple junctions further complicate the deformation mechanism and pose challenges in developing a model that explain the deformation process. In addition, grain growth is always a concern, which limiting the creep temperatures to a low fraction of the melting point [15].

In 1990 [23], Nieman et al conducted constant load creep tests on nc-Pd samples with grain size in the range of 7-10 nm produced by inert-gas condensation at room temperature. The nc-Pd crept at a stress of 148 MPa, which is about 3 times the yield stress of coarse-grained Pd. Their results indicated that diffusional creep was not the determining factor in creep at room temperature.

Table 1.1 The constitutive equations for different creep mechanisms [22].

Mechanism	Constitutive equation
Nabarro-Herring creep	$\dot{\varepsilon} = \frac{14\Omega\sigma}{kT}\frac{1}{d^2}D_l$
Coble creep	$\dot{\varepsilon} = \frac{14\pi\Omega\sigma}{kT}\frac{\delta}{d^3}D_{gb}$
Grain boundary sliding (lattice diffusion controlled)	$\dot{\varepsilon} = 8\times10^6 D_l \frac{Gb}{kT}(\frac{b}{d})^2(\frac{\sigma}{G})^2$
Grain boundary sliding (grain boundary diffusion controlled)	$\dot{\varepsilon} = 2\times10^5 D_{gb} \frac{Gb}{kT}(\frac{b}{d})^3(\frac{\sigma}{G})^2$
Dislocation creep	$\dot{\varepsilon} = 3.83\times10^5 D_l \frac{Gb}{kT}(\frac{\sigma}{G})^n$

Hahn and Averback [24] studied the compressive creep response of TiO_2 at temperatures between 873 and 1073 K. Grain size increased from the original 40 nm to 120 nm and 1000 nm at a total strain of 0.35% and 0.6 %, respectively. The corresponding temperatures are 964 K and 1073 K. They found that the stress exponent is about 3 and the grain size dependence ranging from 1 to 1.5. Based on their results, they suggested that the creep deformation occurred by an interface reaction controlled mechanism.

Wang et al [25] and Deng et al [26] conducted tensile creep tests to study the same Ni-P alloy with a grain size of 28 nm in the temperature range of 543~593 K. The samples were prepared by direct crystallization of amorphous ribbons, which has an advantage over the powder compacted processes in that the experimental data aren't affected by the porosity. They also performed creep tests on Ni-P samples with a grain size 257 nm for comparison. Wang et al found that the apparent activation energy for 28 nm and 257 nm Ni-P is 0.71 and 1.1 eV, respectively. Deng et al found the stress exponent for 28 nm Ni-P

is 1.2, while 2.5 for 257 nm Ni-P. According to the analysis of the creep data, they suggested that the creep of nc-grained sample is controlled mainly by grain (and or phase) boundary diffusion. By contrast creep of the coarse-grained samples is controlled by a combined mechanism involving dislocation creep.

Sander et al [27] carried out creep tests on nc-Pd, nc-Cu and nc-Al-Zr produced by inert gas condensation and compaction over a temperature range of 0.24-0.64 T_m at different stresses. The experimentally observed creep rates were two to four orders of magnitude lower than the values predicted by Coble creep. They attributed the measured low strain rates to the prevalence of low-energy grain boundaries together with inhibition of dislocation activity by small grain size.

Room temperature grain size dependence of steady state creep in electrodeposited nc-Ni was studied by Wang et al [22]. They concluded that at high stress levels, grain boundary sliding becomes the major deformation mechanism at room temperature for nc-Ni. The contribution from diffusional creep mechanism through intercrystalline regions can be significant for smaller grain size. In contrast, Yin et al [28] investigated the creep behavior of nc-Ni with a grain size 30 nm at elevated temperatures in a load range of 500-1050 MPa. Stress exponent was measured to be 1 for 290 K and 6.5 for creep at 373 K. They concluded that the creep deformation at 290 K is dominated by Coble creep mechanism. At 373 K, the creep deformation mechanism might be multiple i.e. lattice dislocation gliding and grain boundary sliding, but the dominated one was not identified.

Cai et al [29-30] studied creep behavior of nc-Cu produced by eletrodeposition and cold-rolling in the temperature range of 293-323 K. The steady state creep rate of

electrodeposited nc-Cu was found to be proportional to the effective stress $\sigma_e = \sigma - \sigma_{th}$, where σ is the applied stress, σ_{th} is the threshold stress. Using σ_e, the creep rates were found to be of the same order of magnitude as those calculated from Coble creep equation. The activation energy for creep was measured to be 0.72 eV, which is close to that of grain boundary diffusion in nano-sized Cu. Their results suggested that the low temperature creep of nc-Cu can be attributed to the interface controlled diffusional creep. However, Li et al [31] refuted the result of Cai et al [29] by attributing the high value of minimum creep rate to premature fracture. For the cold rolled nc-Cu [30], the creep mechanism was found to be associated with grain boundary sliding.

Ogino [32] compared the lower strain rate observed experimentally with the theoretically values predicted by Coble creep. He derived a modified equation of grain boundary diffusional creep which accounts for the increase in grain boundary area due to the deformation of grains at an initial stage of creep. The application of this model to creep of nc-Cu indicates that the creep behavior of nc-materials should significantly deviate from Coble creep as grain size decrease to nanoscale size. Grabovetskaya et al [33] studied the creep features of nc-structured Ni, Cu and Cu-Al_2O_3 produced by severe plastic deformation, they found that power-law equation could describe the steady state creep rate of these three materials satisfactorily.

Lately, Yin et al [34] studied the effect of interstitials on the creep of electrodeposited nc-Ni with a grain size of 30 nm. Their results shown that both minimum creep rate and creep strain significantly decrease with increasing sulfur or by doping boron in nc-Ni. The stress exponent increased to about five at 373 and 473 K from two at room

temperature. A grain boundary sliding model with introducing of grain boundary dislocations and back stress was proposed to explain the large stress exponents. The calculated back stress indicates that the interstitials in grain boundaries effectively retard the sliding of grain boundary dislocations. Interestingly, Kottada et al [35] conducted constant load compressive creep tests on nc-Ni with grain size of ~40 nm. The results revealed extensive primary creep regions and no evidence for steady state deformation. The lack of any change in texture coupled with grain growth suggests that grain boundary sliding/migration/rotation accompanies intergranular dislocation creep.

Creep behavior of nc-materials has been extensively studied not only by experiments but also by simulation. Several models for creep of nc-materials have been proposed based on molecular dynamic simulations. Yamakov et al [36] simulated fully three-dimensional (3D), model nc fcc metal microstructures to study grain-boundary diffusion creep. The simulations were performed at elevated temperatures where the distinct effects of grain boundary diffusion are clearly identifiable. The input microstructures were tailored to prevent grain growth. The simulations revealed that under relatively high tensile stresses these microstructures, indeed, exhibit steady-state diffusion creep that is homogeneous, with a strain rate that agrees quantitatively with that calculated by the Coble creep formula. The grain-size scaling of the Coble creep was found to decrease from third power to second power when the grain diameter becomes of the order of the grain boundary width. A direct observation of the grain boundary sliding as an accommodation mechanism for the Coble creep, known as Lifshitz sliding, was also reported. In the simulation work done by Haslam et al [37], effects of grain growth on

grain boundary diffusion creep and grain boundary sliding during high-temperature deformation of a nc-Pd model microstructure were studied. The initial microstructure is polycrystal consists of 25 grains with an average grain size of about 15 nm and a columnar grain shape. Prior to the onset of significant grain growth, the deformation proceeds via the mechanism of Coble creep accompanied by grain-boundary sliding. While grain growth is generally known to decrease the creep rate due to the increase of the average grain size, the results obtained in their study revealed an enhanced creep rate at the onset of the grain growth, when rapid grain-boundary migration occurs. The enhanced creep rate was shown to arise from topological changes during the initial growth phases, which enhance both the stress induced grain boundary diffusive fluxes and grain boundary sliding. Dislocations generated as a result of grain rotation induced grain coalescence and grain boundary decomposition in the vicinity of certain triple junctions were also shown contribute to the deformation.

It is observed that there is no consensus about the creep results from different sources, some even conflict with others. However, the power-law creep equation is commonly applied to analyze the creep behavior. Most recently, Chokshi [38] developed two modifications specifically for nc-materials using the standard approaches to diffusion transport. These two modifications indicate that unusual grain size and stress dependencies may be observed in nc-materials creep at high stress and low temperatures, i.e. a stress exponent higher than 1 or strain rate is inversely proportional to the grain size for dislocation creep. Thus, it is necessary to be cautious in interpreting creep data for nc-materials.

1.2.2 Indentation Creep of Materials

The flow stress of a material depends on the applied strain rate and temperature, the hardness of a material is expected to follow a similar dependence, resulting from the Tabor relationship between hardness and flow stress [39]. The time and temperature dependent properties can be measured by a variety of techniques. Generally they fall in two classes: 1) conventional microhardness test and 2) depth-sensing techniques.

Among the earliest attempts to gain the insights of the time and temperature dependence of hardness was the hot hardness test. This test was conducted on a standard microindentation system with some modification for using at elevated temperature.

In 1957, Pomey et al [40] found that there was a linear relationship between log (hardness) and log (time). The slope of the double-logarithmic hardness and time curve is temperature dependent, specifically, the slope increases with increasing temperature. In 1960, Mulhearn and Tabor [41] also found the linear relationship between log (hardness) and log (time) for a loading time exceeds a few seconds. This relationship, however, was found to be independent of temperatures and the results were explained in terms of viscous creep.

The conflicting results from independent studies led to the investigation of the indentation hardness and the creep of solids by Atkins et al [42]. Atkins et al studied the effect of indenter geometry on the creep response of indium. The results on indium led them suggest that the rate of deformation cannot be associated with geometry of the indenter itself but rather the rate at which elastic/plastic boundary can propagate into the material. In their study, an expression for transient creep for constant stress condition was

used and an expression for hardness and time was arrived which was remarkably similar to that obtained by Mulhearn et al [41].

Sargent and Ashby [43] adopted a variety of analysis techniques to analyze the hot hardness data from self-similar indentation, i.e. indentation using pyramid or cone shape tip and by which the stress exponent and activation energy for creep can be determined. Shen et al [44] studied the indentation creep of Cu-TiC alloys with grain size from 55 to 100 nm. They found that the activation energies at intermediate temperature ranges were close to those for grain boundary diffusion of Cu. However, the strain rate significantly decreases with decreasing grain size. Based on the results, they concluded that creep mechanism for Cu alloys was a dislocation mechanism controlled by grain boundary diffusion.

The beginning of employing depth sensing technique to study the time dependent properties of materials dates back to late 80s. Four types of tests have been employed to gain insight of the relationship between indentation strain rate and hardness: indentation load relaxation tests, constant rate of loading tests, constant load indentation creep tests and impression creep tests. A detailed review can be found in [45].

Lucas et al [45] applied a variety of depth sensing techniques to study the creep response of high purity indium in a temperature range from room temperature to 348 K. The apparent activation energy for indentation creep was found to be 78 kJ/mol, which is in accordance with the activation energy for self diffusion in the material. The stress exponent was found to be similar by different loading schemes. The most important

finding in their study was that a constant indentation creep rate can be obtained during an experiment by keeping the loading rate divided by load constant.

Followed Lucas et al's work, many studies have been focused on using nanoindentation techniques to study creep behavior of a variety of materials. Chudoba et al [46] investigated the creep behavior of different substrates and film combination materials. Their results showed that the creep during nanoindentation can be reproducibly determined with an accuracy better than 1 nm, if the drift rate under measurement was corrected. A logarithmic formula can well describe the observed creep for all materials. They further pointed out the loading time and the hold period of the load can have a strong influence on hardness and modulus. The influence of loading rate or displacement rate on the results can be avoided by choosing appropriate holding time for different film-substrate combination.

Feng and Ngan [47] studied the creep and strain burst in indium and Al by nanoindentation technique. They found that in Al, strain burst was necessary for creep to occur. Creep occurs as soon as a strain burst appears. While for indium, creep can take place before or after strain burst. The stress exponent changed from ~1.5 before strain burst to ~6 after strain burst suggested that the creep mechanism was diffusional creep before strain burst and dislocation creep after. Strain burst was also found in the creep of Cu film under nanoindentation creep by Wang et al [48]. The stress exponent change from 8.3 before strain burst to 6.3 after at a creep load of 2 mN. They attributed this change to the difference in dislocation density before and after the strain burst. The stress exponent was found to increase with increasing applied load.

Li and Ngan [49] studied room temperature indentation size effect of nanoindentation creep for three kinds of materials: single-crystal Ni_3Al, polycrystalline pure Al and fused quartz samples. The stress exponents of constant load indentation creep in the three materials were found to be small at small loads. In Al and fused quartz, the stress exponent measured for small indents approach unity. The stress exponent in all the three materials increased rapidly as the indent size increases. For the two crystallized materials, the change of stress exponent with size signified a mechanism transition. The reduction in the localized shear volume could be reason for the observed size effect in the amorphous quartz.

With the advancement of indentation techniques and sample preparation methods, nanoindenter has been customized to study the creep behavior of micro-sized Ni_3Al pillars under different compressive loads [50]. The nominal creep rate was found to be in the order of 10^{-5} s^{-1}. The stress exponent of these pillars was found to be close to 1, indicating the creep mechanism was diffusional creep. The microscopic evidence suggests deformation was due to the surface diffusion at the top of the pillars.

The creep behavior of nano-scale Ag-Co multilayers produced by magnetron sputtering with a periodicity of 4-60 nm was also studied by indentation creep[51]. Dimensional analysis has shown that the stress exponents were in the range of 2.5-5.0, which indicated that dislocation climb was a possible deformation mechanism for indentation creep. A constant rate indentation creep tests were carried out by Ma et al [52] on nc-Ni with an average grain size of 25 nm. The creep rate, creep strain rate, indentation stress and stress exponent were found to be indentation depth dependent. It was inferred

that the creep was likely dominated by grain boundary sliding and a grain rotation mechanism for small indents but by dislocation climb for large indents.

1.2.3 Correlation of the Uniaxial Creep and Indentation Creep

Uniaxial creep and indentation creep can be conducted independently to obtained insight about the creep responds of materials as described in sections 1.2.1 and 1.2.2. However, a direct comparison of data obtained from the two tests is not avoidable.

Muhmudi et al [53] showed that the stress exponent of Sn-40%Pd-2.5%Sb determined through indentation creep agreed well with that obtained by conventional creep. However, Goodall and Clyne [54] found a poor correlation between their data and those in the literature. The discrepancy might be due to the fact that the data were from different sources and the microstructure of the materials was different. In addition, test temperature range might play a key role in the comparison. Lucas and Oliver [45] carried out nanoindentation creep experiments on In and observed a stress exponent of 5, which was similar to that reported for In under uniaxial creep [55]. The magnitude of the two creep strain rates differed greatly, but the reason was not given. Poisl et al [56] made efforts to correlate indentation creep rate to the effective creep rate experienced by the material under the indenter. It is necessary to point out that Poisl et al studied amorphous Se, which behaved like a Newtonian flow at temperatures above its glass transition temperature. The linear relationship between strain rate and stress for Newtonian flow made the determination of correlation coefficient $\beta = \dot{\varepsilon}_u / \dot{\varepsilon}_I$ ($\dot{\varepsilon}_u$ is uniaxial creep rate, $\dot{\varepsilon}_I$ is indentation rate) relatively easy, and β =0.09 in their study. For crystalline material, however, the determination of β is not straightforward since the stress exponent is usually

not unity. It is pertinent to conduct uniaxial creep and indentation creep on the same materials and using the same equipment, and directly compare the data obtained from the two tests to find the value of β.

1.3 Deformation Behavior of nc-Materials

Cyclic deformation behavior of microcrystalline materials has been the subject of considerable research for the past four decades [57-59]. Pure metals may harden or soften depending on their initial structures when they subjected to cyclic plastic strain. Cyclic softening or cyclic hardening generally observed and has been extensively studied. The hardening mechanisms explained by correlating the applied cyclic stress or strain amplitude with stress-strain hysteresis and saturation responses and the evolution of energetically favorable dislocation structures [60-62]. However, the study of cyclic deformation behavior of nc-materials in open literature is still in its early stage.

Among the earliest work on cyclic deformation of nc-materails, Moser et al [63] studied the cyclic loading behavior of nc-Ni with an average of about 30 nm produced by electrodeposition. In their experiments, nc-Ni was subjected to tension-tension cyclic deformation, they found that cyclic strain hardening for the first time in nc-Ni, the majority of the hardening appears during the early stages of cyclic deformation. The early stages hardening was attributed to dislocation sources exhaustion and later stages hardening to time-dependent, irreversible grain boundary processes. Chen et al [64] also conducted cyclic loading tests on nc-Ni. The grain size of Ni in their study was 20 nm. The cyclic loading was performed under constant load-controlled mode. In contrast to Moser et al's results, Chen et al observed strain softening i.e. an increase of macroscopic strain with

cycle number. The different observations in both investigations might relate to the different initial structure of nc-Ni and the test condition.

Recently, multistep load-unlaod nanoindentation was employed to address the effect of deformation-induced microstructural evolution on mechanical behavior of nc-Ni [65]. In their study, Pan et al compared the hardness measured from single step and multi-step indentation tests. They observed a weak hardening at a highest loading rate of 70.6 mN/s and a slight difference in material response between the multi-step and single step profiles at medium loading rates. At the slowest loading rate of 1.32 mN/s, considerable softening occurred in nc-Ni during multi-step nanoindentation comparing with that of single step test. This softening was attributed to the grain growth induced by deformation, either through stress-assisted grain boundary migration or grain rotation[66-67] .

Saraswati et al [68] conducted cyclic nanoindentation tests on 5N pure Au and Ca-doped Au rods. Their results showed that there was a disparity between unloading and reloading paths. This disparity depended on both dopant level and nanoindentation depth and was attributed to interactions between Ca and defects such as dislocations and grain boundaries during interrupted loading.

In most work done on cyclic deformation behavior of materials, usually cyclic fatigue was characterized, and the frequency and stress effect on the magnitude of the strain in each cycle were studied. For materials with grain size in the micro-sized range or larger, many deformation mechanisms contribute to the observed hysteresis of the materials, which make it not easy to model the deformation mechanism since they operate concurrently and the way they interact with each other and the sequence they occur

whether in series or parallel or both are unknown. However, it is generally recognized that dislocation-mitigated process is limited during plastic deformation of nc-metals with a grain size less than about 50 nm [12, 69-71]. Resulting from extremely small grains, nc-materials have a high volume fraction of grain boundaries. Plastic deformation in nc-metals is mainly controlled by facile grain-boundary processes such as grain boundary sliding[72] , grain migration and rotation [67, 73]. The dominant deformation mechanisms involved in nc-materials are grain boundary processes, especially grain boundary sliding. Since the constitutive relation describing the grain boundary sliding has been well developed, it is feasible to build mechanistic model to describe the cyclic i.e. unload-reload behavior of nc-materials from the view point of grain boundary sliding.

1.4 Objectives of Study

It has been shown that both uniaxial and nanoindentation creep have been independently and successfully conducted to gain insight of creep behavior of nc- materials. Generally, stress and temperature dependence of the two tests were found similar. However, the large discrepancy in the creep rate measured by the two tests is still unclear. So does the way how stress and strain affect the grain boundary related mechanical hysteresis in nc-materials. The overall objective of the proposed research is to study the mechanical behavior of nc-Ni using nanoindentation techniques. Various experimental and characterization techniques will be employed in order to achieve this aim. Scanning electron microscopy (SEM) will be used to observe the morphology of the pillar samples before and after deformation. Focus ion beam (FIB) technique will be employed not only to produce micropillars for microcompression tests but also to prepare the transmission

electron microscopy (TEM) samples after nanoindentation. X-ray diffraction (XRD) technique will also be used as a supplement to TEM. These experimental approaches fulfill the following objectives: 1) gain a better understanding of the creep behavior of nc-Ni, especially stress and temperature dependence under nanoindentation creep (complex stress states) and uniaxial microcompression creep (simple uniaxial stress) at elevated temperatures, and determine the rate controlling mechanism; 2) correlate the uniaxial creep data with nanoindentation creep data; 3) investigate the mechanical hysteresis behavior of nc-Ni. The effect of stress magnitude, stress state, strain rate and grain size on the hysteresis behavior will be studied in terms of grain boundary process related energy dissipation. A mechanistic model based on grain boundary sliding will be proposed to describe the unload-reload behavior.

Chapter 2 Material Preparation and Experimental Techniques

2.1 Material Preparation

In this study, nc-Ni is selected for the study of the mechanical behavior at both ambient and elevated temperatures. This attributes to the following four reasons. First, it can be readily synthesized over a wide range of grain sizes, which is necessary for examining the deformation mechanism transition behavior. Second, it doesn't oxidize until temperature higher than 400-500^{o}C. Third, it has relative high stacking fault energy which makes it less likely to form twins during manufacture. Last, the thickness of deposited Ni film is thick enough to prepare free standing microcompression samples.

Nc-Ni films with grain sizes of 14 and 43 nm were obtained from the Himeji Institute of Technology, Himeji, Japan, by direct current electrodeposition in a Ni sulfate based bath. After finish deposition, the deposited films were separated from their substrates by immersing them into a mixture of chromium hemitrioxide and sulfuric acid. Ni films with grain size of 65 nm were obtained from The Hong Kong Polytechnic University. In this case, stainless steels were used as substrates. The nc-Ni films were mechanically separated from the substrates after deposition. The thickness of all films is about 100 μm. Hereafter, samples with grain size of 14, 43 and 65 nm are denoted as Ni14, Ni43 and Ni65, respectively.

Samples for nanoindentation were prepared by standard metallurgical procedures. Specifically, each sample was ground with SiC paper from #1200 to #2400 and #4000. The final polishing was done with micro-cloth using a slurry of 1.0 μm alumina. Micropillars for microcompression tests were fabricated by focus ion beam (FIB) on the

surface of the mirror-finishing Ni samples following the prototypical methodology of Uchic et al [74]. The voltage for FIB processing is 30 keV, and the current is in the range of 7-0.09 nA. All pillars were manufactured to have an aspect ratio of 2:1, and a nominal diameter of 2 μm measured at the center height of the pillars. The pillars were made at the center of a 45 μm crater to provide enough space for the flat-ended punch to move down during the test and to guarantee that it only contact the pillar of interest. Dog-bone shaped tensile samples were machined by electrical discharge machining.

2.2 Nanoindentation Creep and Uniaxial Microcompression Creep

Nanoindentation, depth sensing technique or instrumented indentation technique, is a technique developed during the late 80's to early 90's. This technique has been widely used and demonstrated to be a powerful technique in obtaining mechanical properties of materials, especially in the samples with small volume at small scales [75-76]. The primary properties measured are hardness and modulus. Nanoindentation has also been adopted to study the rate dependence processes such as creep [45, 49, 56]. The recent development of high temperature stage facilitates the investigation of temperature dependence of mechanical properties such as creep.

In this study, both nanoindentation creep and microcompression tests were carried out on Triboindenter (Hysitron, Inc., Minneapolis, MN). The indenter system is shown in Figure 2.1 [77]. The Triboindenter has a displacement resolution of 0.04 and 4 nm in Z-axis and X-axis respectively, and a load resolution of 1 nN in Z-axis and 4 μN in X-axis. The maximum indentation depth and maximum load are 5 μm and 12 mN, respectively. For tests conducted at elevated temperatures, a heating stage with a heating capacity to

473 K was attached to the transducer/scanner assembly. The set up of heating stage is shown in Figure 2.2.

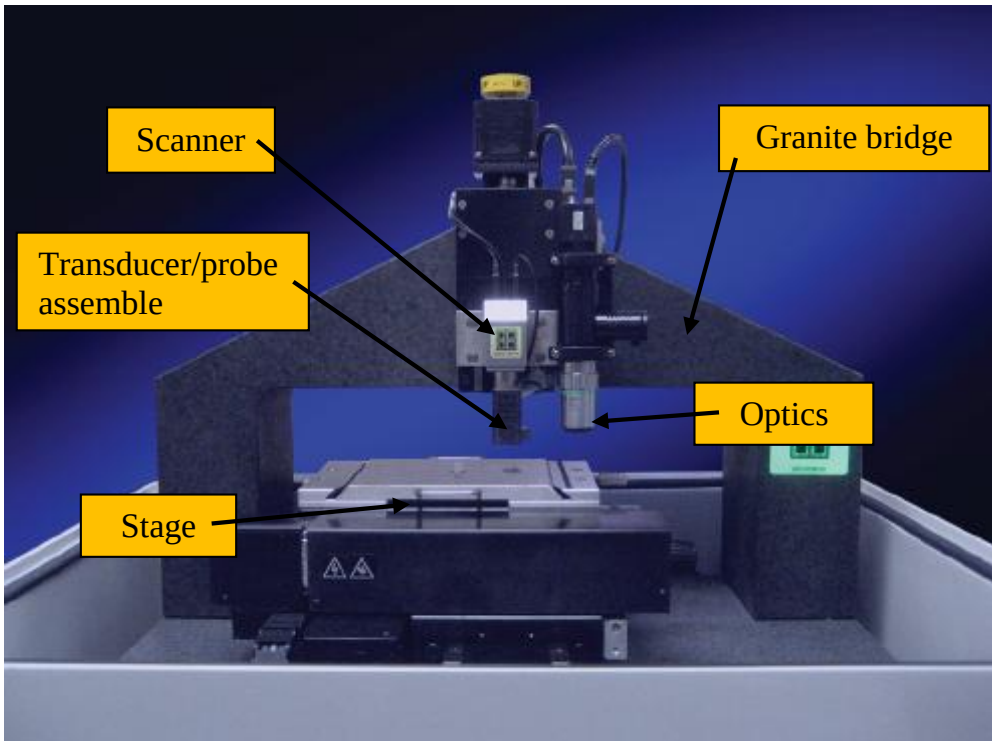

Figure 2. 1 Schematic of Triboindenter [77].

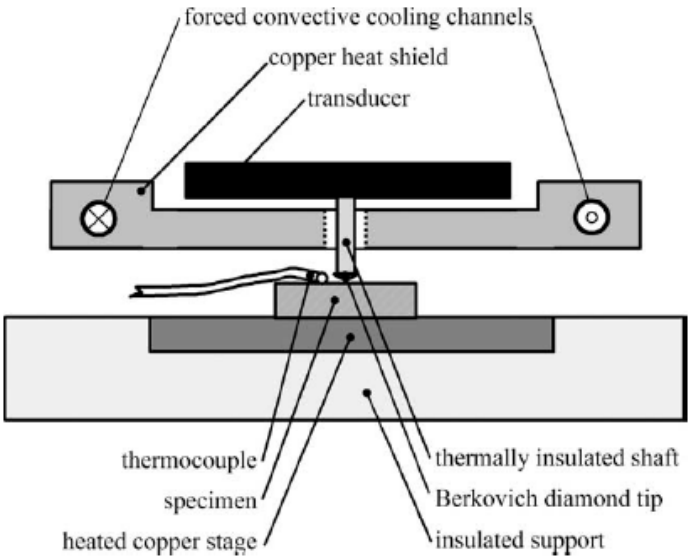

Figure 2.2 Schematic of the elevated temperature nanoindentation set up [78].

2.2.1 Nanoindentation Creep

Nanoindentation creep tests were conducted on Triboindenter using a diamond Berkovich tip mounted on a macor rod which has a centerline-to-face angle, φ, of 65.35^{o} as shown in Figure 2.3. The indentation creep tests were performed at fixed loads of 1, 5 and 9 mN. The loading scheme including three segments, first the specimen was uploaded to a preset maximum load with a fix time of 1 s followed by a holding segment of 30 s to examine the creep behavior. After the holding, the load was immediately reduced to zero. The tests were carried out at temperatures of 348, 398 and 448 K to study the temperature dependence of the creep. Each test was conducted on a single specimen, but the test at each condition was performed at least 5 times, the reported values are the average. Prior to tests, the Triboindenter and tip were carefully calibrated using standard sample.

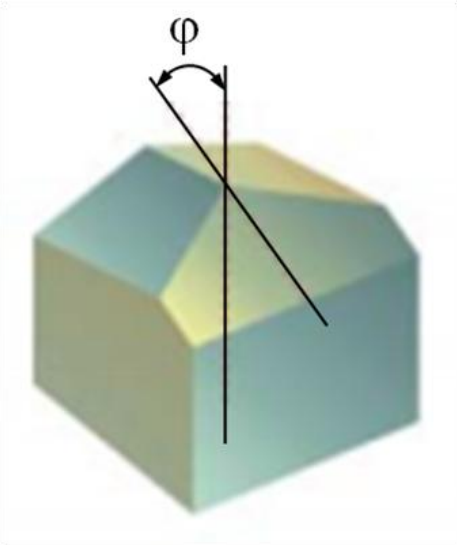

Figure 2.3 Berkovich tip for nanoindentation, face angle $\varphi = 65.35^{o}$ [79].

2.2.2 Uniaxial Microcompressive Creep

The uniaxial creep tests were conducted on the same Triboindenter as that for nanoindentation creep. In contrast to a Berkovich tip used for nanoindentation creep, the flat-ended punch was used for microcompression tests, which was machined out of a standard diamond Berkovich tip. The resulting punch has an equal lateral triangle cross section with an about 8 μm inscribed circle as shown in Figure 2.4. The side view in Figure 2.4 (b) indicates the flatness of the end surface of the flat-ended punch. Microcompression tests were conducted under imaging mode, which provides a direct view of the top of the pillar and offer the ability to precisely positioning the flat-ended punch at the center of the pillar. The loading and unloading time is 1 s and the dwell time at peak load is 60 s. The peak loads is in the range of 3.6 to 5 mN. The data from uniaxial creep were analyzed using conventional power-law relationship.

2.2.3 Thermal Drift

For nanoindentation tests, especially at elevated temperatures, thermal drift is always a concern. Efforts were made to reduce and quantify this effect. Prior to each test and after stabilized at a prescribe temperature for at least 15 minutes, the indenter tip was brought into contact with the sample surface so that the tip can reach a steady-state temperature distribution. In addition, thermal drift was automatically corrected by the Triboindenter software during testing. Furthermore, the drift rate effect on the creep behavior was estimated by considering it analogous to a one-dimensional random walk problem, i.e. displacement changes with square root of the time instead of linear change with time as described in [80].

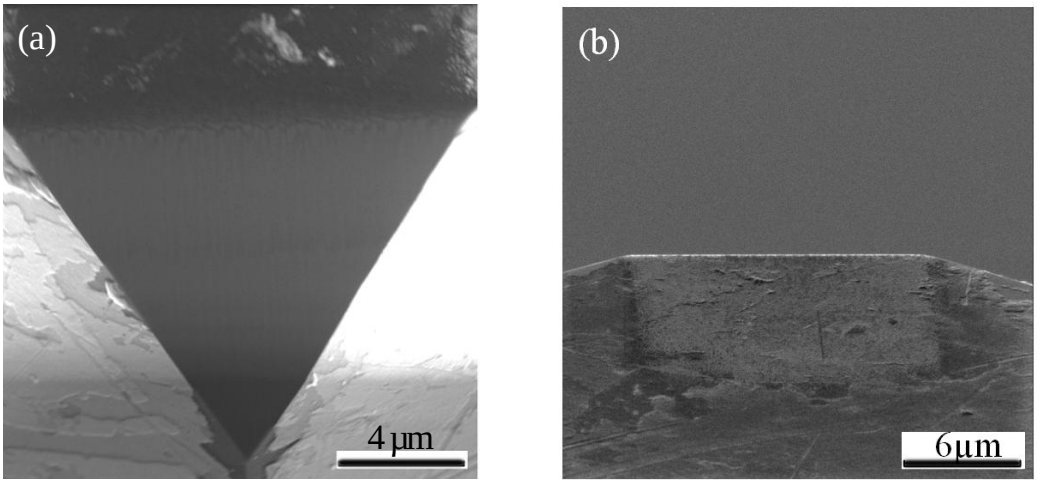

Figure 2.4 SEM micrographs of a flat-ended punch after FIB milling (a) top view and (b) side view

2.3 Cyclic Unload-Reload Tests

2.3.1 Cyclic Unload-Reload Microcompression Tests

In order to study the mechanical hysteresis behavior of nc-Ni, cyclic microcompression tests of Ni pillars were also performed on Triboindenter (Hysitron, Inc., Minneapolis, MN) using the same flat-ended punch as that for microcompression creep. The tests were conducted at ambient temperature. The pillar samples with as-deposited grain size of 65 nm were deformed under a displacement control mode with nominal strain rates of 5×10^{-4}, 10^{-3} and 10^{-2} s^{-1}. In microcompression, pillars were initially compressed to a displacement of 100 nm before the first unloading. In the subsequent unload-reload cycles, the pillars were strained to 200, 300, 400, 500, 600 and 700 nm. After a peak displacement of 700 nm, the load was reduced to zero. The unloading of each cycle was carefully controlled such that the punch always making intimate contact with the top surface of the pillar. Prior to each test, the apparatus was finely tuned and aligned to avoid misalignment.

2.3.2 Cyclic Unload-Reload Tensile Tests

Cyclic unload-reload tensile tests were also performed to study the mechanical hysteresis of nc-Ni. Tensile tests were carried out on Instron 5566 universal testing machine. Dog-bone shape samples with gage length of 6 mm and width of 3 mm were prepared by electrical discharge machining. The tests were conducted at the same nominal strain rate range as that in compression. The samples were loaded to preset displacement with equal increment between two cycles. For the unloading segment of each cycle, the stress was reduced to 20 MPa except for the last cycle to zero. There was no holding time

between each unloading segment and its following reloading segment. One FLA type strain gage (3.5 mm × 1.6 mm) from Tokyo Sokki Kenkyujo Company with epoxy backing was attached to the gauge section of each tensile sample by metal epoxy. Before each test, the sample was held in tension by a few Newton for about 10 to 15 minutes to allow the strain gage to equilibrate, after which the load and strain were electronically balanced to zero. This setup allows a direct measurement of sample strain, eliminating the need to account for machine compliance. Strain and time from strain gage were measured using a signal conditioning amplifier from Vishay Micromeasurement Company. The collected data from strain gage were input into the data collecting software labview. The load during tensile test was measured by the load cell of the Instron machine.

2.4 Observation of Microstructure and Morphology of Samples

The grain size of the as-deposited Ni films was determined using both X-ray diffraction operated at 45kV and 40 mA and Philips CM300 transmission electron microscopy (TEM). The morphology of the pillars before and after deformation was examined by LEO scanning electron microscopy. Samples for microstructural examination after nanoindentation were also prepared by FIB technique using trench and lift-out technique (FEI Helios 600 dual beam FIB/SEM system, FEI Inc., Hillsboro, OR). The microscope was equipped with a scanning TEM (STEM) detector allowing high contrast STEM imaging with a resolution of 0.8 nm. The TEM investigations were performed using a Philips EM430 microscope (FEI Inc., Hillsboro, OR) operated at 300kV.

Chapter 3 Nanoindentation Creep of nc-Nickel at Elevated Temperatures

This chapter is a slightly revised version of a paper entitled "Nanoindentation creep of nanocrystalline nickel at elevated temperatures" published in *Journal of Physics D: Applied Physics* in 2009:

C L Wang, M Zhang and T G Nieh, Nanoindentation creep of nanocrystalline nickel at elevated temperatures, *Journal of Physics D: Applied Physics* 42 (2009) 114505-1-8.

The use of "we" in this chapter refers to my co-authors and myself. My primary contributions to this paper include (1) most of the experiment work, (2) most of the data analysis, (3) most of the writing.

In order to obtain thorough understanding of creep behavior of nc-Ni under nanoindentation creep (complex stress states) at elevated temperatures, nanoindentation creep of nc-Ni was conducted in the temperature range of 348 – 448 K using a Berkovich tip. The creep peak load was in the range of 1-9 mN with a loading/unloading time of 1 s and a peak load holding duration of 30 s were applied. The temperature and load dependence of creep was studied. Possible creep mechanisms were discussed in light of the calculated stress exponent, creep rate, activation volume and activation energy. Room temperature stress relaxation test was also conducted to evaluate the temperature's contribution to the activation volume.

Properties of nc-materials highly depend on their microstructure. Effort was made to characterize the grain size of Ni foil at the beginning of the creep using XRD pattern.

The microstructure of nc-Ni after nanoindentation was observed by TEM. A cross section sample cross the indent was prepared by FIB technique.

3.1 Results from Nanoindentation Creep of nc-Ni

During nanoindentation, the load and displacement are simultaneously recorded as a function of time. The displacement -time curve for nc-Ni crept at 348 K under a load of 9 mN is presented in Figure 3.1. For self-similar indentation tip like Berkovich tip used in the current study, the following relationships are applied to obtain indentation creep rate $\dot{\varepsilon}_I$ [49] and indentation hardness H [75].

$$\dot{\varepsilon}_I = \frac{1}{h}\frac{dh}{dt} = \frac{\dot{h}}{h} \tag{3-1}$$

$$H = \frac{P}{Ch^2} \tag{3-2}$$

where $\dot{h}$ is the displacement rate of the tip, h is the instantaneous indenter displacement, P is indentation load, C is a constant determined by the shape of the tip, and H is the hardness. The displacement rate $\dot{h}$ at a constant creep load, can be obtained either by measuring the slope of displacement-time curve as that shown in Figure 3.1 or by fitting the displacement-time curve using an empirical equation:

$$h(t) = h_0 + a(t - t_0)^p + kt \tag{3-3}$$

here, h_0, a, t_0, p and k are fitting constants. An example of determining these fitting parameters is presented in the inset of Figure 3.1. Indentation creep rate $\dot{\varepsilon}_I$ can be computed by taking the time derivative of the fitted displacement-time curve, i.e.

instantaneous displacement rate and dividing it by the displacement at any particular point in time.

Fitted displacement-time curves for Ni14 crept under a fixed load of 9 mN at different temperatures are presented in Figure 3.2(a). The origin of each curve is set to be the starting point of creep. It is evident in Figure 3.2(a) that creep displacement is larger at a higher temperature, which is expected since creep is a thermal activated process and higher temperature promotes a faster diffusion. Similar trend was also observed at the other two loads, 1 and 5 mN. Following the same procedure, fitted curves for Ni14 crept at a constant temperature of 448 K but under different loads are presented in Figure 3.2(b). Creep displacement was observed to increase with applied load at a fixed temperature. The shape of the displacement-time curves in Figure 3.2 is particularly noted to be similar to the shape of the strain-time plot (i.e. creep curve) reported for conventional creep of polycrystalline metals.

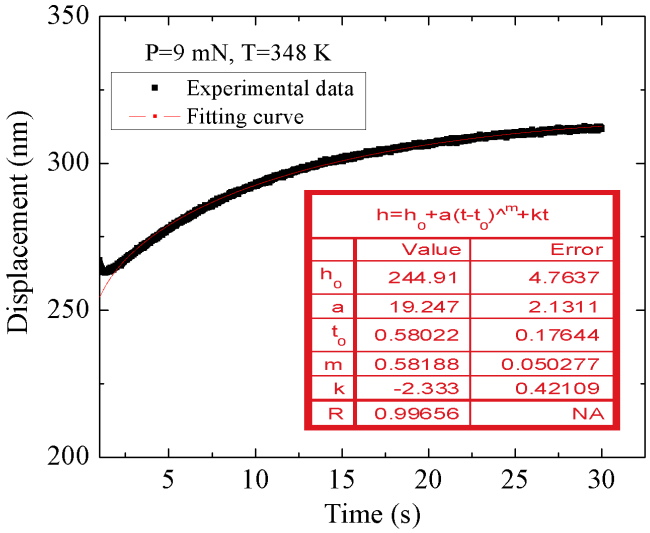

Figure 3.1 Creep displacement-time curve for nc-Ni crept at 348 K and 9 mN.

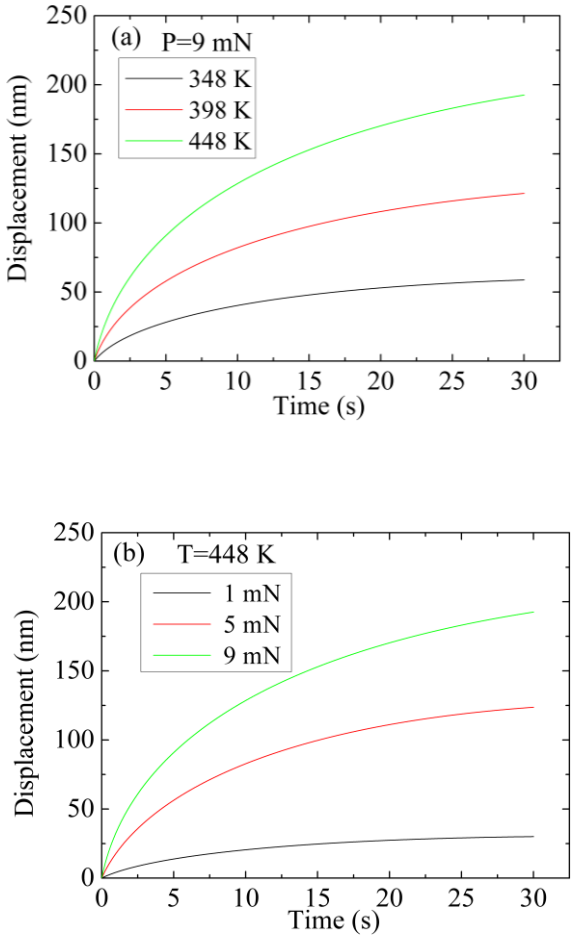

Figure 3.2 Nanoindentation displacement as a function of time for Ni14. Creep tested at (a) 9 mN under different temperatures, and (b) 448 K under different peak loads.

Using data in Figure 3.2 the indentation creep rate $\dot{\varepsilon}_I$, at a fixed load of 9 mN was calculated using equation (3-1) and plotted as a function of time in Figure 3.3 for Ni14. In Figure 3.3, $\dot{\varepsilon}_I$ is noted to decrease rapidly in the beginning and reaches an apparent steady state with the creep rate on the order of about 10^{-3} s^{-1}. The transient time from the primary

to steady-state creep, i.e. the primary creep region, is observed to increase with the test temperature, which is explained as follows.

It was reported that, when creep of an alloy obeys the power-law relationship, the primary creep strain can be expressed as [81]:

$$\varepsilon = (\frac{\sigma}{K})^{\frac{1}{N+m}} (\frac{N+m}{m})^{\frac{m}{N+m}} t^{\frac{m}{N+m}} \quad (3\text{-}4)$$

where K is a material strength parameter, N is the strain hardening exponent, and m is the strain rate sensitivity (SRS). In general, when temperature increases, N decreases but m increases. The flow index ($m/N+m$) is, therefore, increased with increasing temperature. This leads to a conclusion that, at a fixed applied stress (or load), the primary creep strain increases with increasing temperature, as demonstrated by the current data in Figure 3.3.

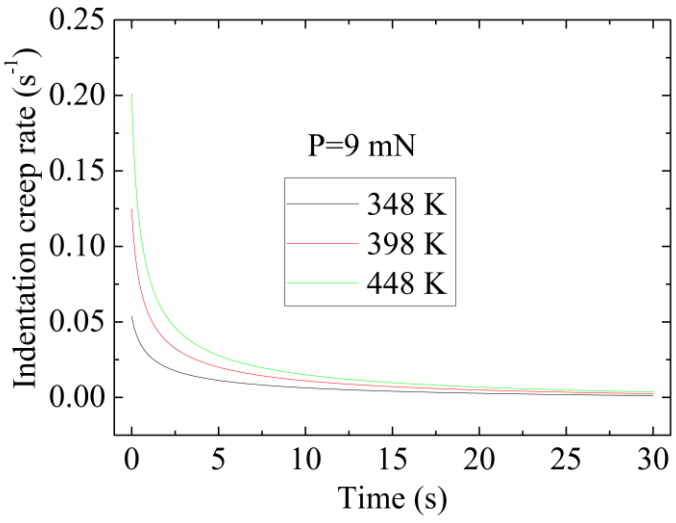

Figure 3. 3 Indentation creep rate as a function of time at 9 mN for Ni14.

3.2 Stress Dependence

The indentation creep rate $\dot{\varepsilon}_I$, stress σ, and temperature T are empirically correlated through a power-law creep equation [82]:

$$\dot{\varepsilon}_I = A\sigma^n \exp(-Q/RT) \tag{3-5}$$

where A is a structure-dependent constant and *n* is the creep stress exponent, which is the inverse of SRS (i.e. $n = 1/m$). Combing equations (3-1) and (3-2), a relationship between strain rate and hardness change rate is readily deduced as

$$\dot{\varepsilon}_I = -C\dot{H}/H \tag{3-6}$$

where C is a material parameter. Using Tabor relationship $H = \alpha\sigma$, where $\alpha \approx 3$ for nc-Ni [83], substituting equation (3-6) into equation (3-5), and integrating with time, the hardness change as a function of holding time can be described by [44]

$$\ln(H^{-n} - H_0^{-n}) = \ln B - Q/RT + \ln(t - t_0) \tag{3-7}$$

where $B(= nA/c^n\beta)$ is a structure-dependent constant. At a fixed temperature and under the usual assumption of $H^n << H_0^n$, equation (3-7) is deduced to a result that $\ln H$ is linearly scaled with $\ln(t - t_0)$. In addition, the slope of the $\ln H$ versus the $\ln(t - t_0)$ plot gives the SRS value $(1/n)$. As shown in Figure 3.4, data from Ni14 deformed under a fixed load of 9 mN at different temperatures indeed obey a linear relationship. Following similar procedures, the *n* values for Ni14 crept at various temperatures and loads were obtained and tabulated in Table 3.1. The effect of thermal drift on the measurement of stress exponent *n* was presented in Table 3.1 also. It is noticed that the estimated error ranges from 0.6 to 18% with a typical value of about 5%, which is reasonably small. The

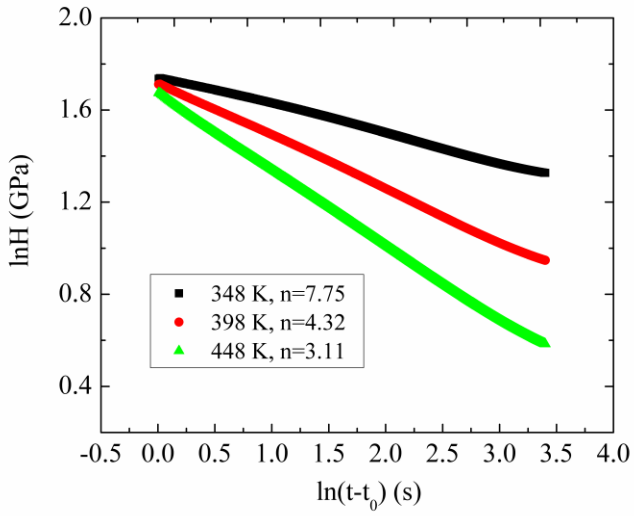

Figure 3.4 lnH-ln(t-t_0) for Ni14 crept under a fixed load of 9 mN.

Table 3.1 Summary of creep stress exponent *n* and activation volume V for Ni14 crept at different temperatures and applied loads. Errors caused by thermal drift are included in the parenthesis. Activation volume is expressed by the dimensionless quantity V/b^3.

	348 K		398 K		448 K	
	n	V/b^3	*n*	V/b^3	*n*	V/b^3
1 mN	14.81(±18%)	3.78	7.14 (±7.3%)	2.74	4.91 (±4.4%)	2.48
5 mN	9.62 (±4.5%)	3.34	4.67 (±1.7%)	2.47	3.27 (±1%)	2.52
9 mN	7.75 (±2.5%)	2.98	4.32 (±1.1%)	2.51	3.11(±0.6%)	2.68

step by step derivation of the thermal drift effect on the sensitivity of measurement of stress exponent is presented in the next section.

It is noted in the Table 3.1 that *n* generally decreases with increasing temperature and applied creep load. A decreased *n* value (or increased *m* value) with increasing temperature is understood by the fact that more thermal recovery occurs at a higher temperature. Low temperature deformation usually promotes athermal plasticity, which is manifested by a low *m* value. A decreased *n* value with increasing applied load at first appears to be counter-intuitive. However, it is the hardness (or stress) that determines the creep deformation, not the net load. The non-linear relationship between the applied load and contact area (equation (3-2)) produces a net stress which is not proportional to the applied load. In fact, this non-linearity results in the lowest stress at the highest load of 9 mN. Thus, a decreased *n* value with increasing applied load was also expected.

3.3 Thermal Drift Effect on the Measurement of Stress Exponent

Thermal drift is always a major concern for nanoindentation creep, especially for tests conducted at elevated temperatures for extended period of time. Alkorta et al [80] suggested a method to estimate the effect of thermal drift on the resulting SRS i.e. reciprocal of stress exponent. However, the equation $h = \bar{h} - \lambda t$, λ is the thermal drift, used by Alkorta et al represents the upper limit for the thermal drift effect. In reality, the thermal drift effect is expected to be analogous to a one-dimensional random walk problem, i.e. displacement changes with the square root of the time, $h = \bar{h} - \chi\lambda\sqrt{t}$. By adopting

this theorem, the effect of thermal drift on the sensitivity of stress exponent *n* is derived as following. The nanoindentation displacement can be expressed as follows:

$$h = \bar{h} - \chi\lambda t^{1/2} \tag{3-8}$$

where λ is the drift per unit time, h and $\bar{h}$ are indentation displacement with and without thermal drift, respectively, and $\chi \cong 1$, the above equation can be simplified to

$$h = \bar{h} - \lambda t^{1/2} \tag{3-9}$$

The displacement rate can be readily calculated from equation (3-9) as

$$\dot{h} = \dot{\bar{h}} - (\lambda/2)t^{-1/2} \tag{3-10}$$

where $\bar{h}$ and $\dot{\bar{h}}$ are the indentation displacement and indentation displacement rate in the absence of thermal drift. The strain rate sensitivity (SRS), as the load is constant during creep, is

$$m^{-1} = \frac{d\ln(\dot{h}/h)}{d\ln H} = \frac{d\ln\dot{h} - d\ln h}{-2d\ln h} = \frac{1}{2}(1 - \frac{d\ln\dot{h}}{d\ln h}) \tag{3-11}$$

Similarly,

$$\bar{m}^{-1} = \frac{1}{2}(1 - \frac{d\ln\dot{\bar{h}}}{d\ln\bar{h}}) \tag{3-12}$$

where $\bar{m}$ is the SRS without thermal drift.

From equation (3-10), we have

$$d\ln\dot{h} = d\ln[\dot{\bar{h}} - (\lambda/2)t^{-1/2}] = \frac{d\ln\dot{\bar{h}} + [(\lambda/4)t^{-3/2}dt]/\dot{\bar{h}}}{1 - (\lambda/2)t^{-1/2}/\dot{\bar{h}}} \tag{3-13}$$

and

$$d\ln h = d\ln(\bar{h} - \lambda t^{1/2}) = [d\ln\bar{h} - (\lambda/2)t^{-1/2}dt/\bar{h}]\frac{\bar{h}}{\bar{h} - \lambda t^{1/2}} \tag{3-14}$$

Since $d\ln\bar{h}/dt = \dot{\bar{h}}/\bar{h}$, rearrange this equation we get $dt/\bar{h} = d\ln\bar{h}/\dot{\bar{h}}$, insert this equation into equation (3-14) and get rid of $dt/\bar{h}$ leads to

$$d\ln h = \frac{1 - (\lambda/2)t^{-1/2}/\dot{\bar{h}}}{1 - \lambda t^{1/2}/\bar{h}} d\ln\bar{h} \tag{3-15}$$

Then, recalling equation (3-11) and using equations (3-12), (3-13) and (3-15), we obtain

$$2m^{-1} - 1 = (2\bar{m}^{-1} - 1) \cdot f(\lambda, \bar{h}, \dot{h}, t) \tag{3-16}$$

where

$$f(\lambda, \bar{h}, \dot{h}, t) = \frac{1 - \lambda t^{1/2} / \bar{h}}{[1 - (\lambda / 2) t^{-1/2} / \dot{\bar{h}}]^2} \tag{3-17}$$

Taking logarithms on the both sides of equation (3-16), we get

$$\ln(2m^{-1} - 1) = \ln(2\bar{m}^{-1} - 1) + \ln f(\lambda, \bar{h}, \dot{h}, t) \tag{3-18}$$

Then, the change of m with respect to drift λ is

$$\frac{\partial \ln(2m^{-1} - 1)}{\partial \ln \lambda} = 0 + \frac{\partial \ln f}{\partial \ln \lambda} \tag{3-19}$$

or,

$$\frac{\partial \ln m}{\partial \ln \lambda} = \frac{m - 2}{2} \frac{\partial \ln f}{\partial \ln \lambda} \tag{3-20}$$

Use equation (3-17), we get

$$\frac{\partial \ln f}{\partial \ln \lambda} = \frac{\lambda t^{-1/2}}{\dot{h}} \tag{3-21}$$

Insert equation (3-21) into equation (3-20), we finally obtain

$$\left| \frac{\Delta m}{m} \right| = \frac{2 - m}{2} \frac{\lambda t^{-1/2}}{\dot{h}} \frac{\Delta \lambda}{\lambda} = \frac{2 - m}{2} \frac{\Delta \lambda t^{1/2}}{h} \tag{3-22}$$

On the other hand, the sensitivity of the stress exponent, n=1/m, with respect to the thermal drift rate can be written as

$$\left| \frac{\Delta n}{n} \right| = (2\bar{n} - 1) \frac{\Delta \lambda t^{1/2}}{h} \tag{3-23}$$

The effect of thermal drift on the measurement sensitivity of stress exponent was estimated applying equation (3-23) and the values are tabulated in Table 3.1 as shown in the above section.

3.4 Temperature Effect

Activation energy as an indicator of the rate controlling process involved in the deformation can be obtained by plotting $\ln[(H^{-n} - H_0^{-n})/(t - t_0)]$ against the inverse of temperature $(1/T)$ and it is shown in Figure 3.5. Despite some data variations, the activation energy is calculated to be 123.1 kJ/mol for Ni. This value is remarkably close to the activation energy for grain-boundary self diffusion in Ni, 115 kJ/mol [84], but is far less than that for lattice diffusion (284 kJ/mol) [85]. This indicates that the rate controlling process in the current nc-Ni is associated with grain-boundary diffusion not bulk diffusion.

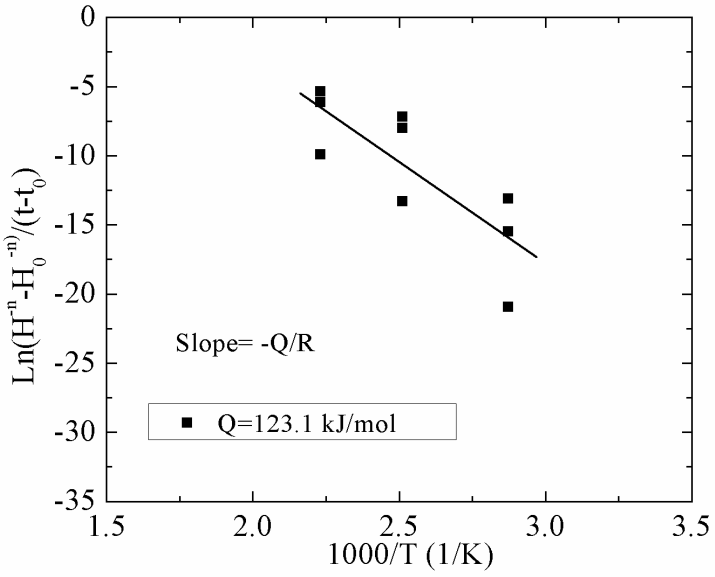

Figure 3.5 $\ln[(H^{-n} - H_0^{-n})/(t - t_0)]$ versus the reciprocal of the absolute temperature. Activation energy can be readily extracted from the slope, which is indicated on the Figure.

3.5 Activation Volume

The activation volume, V, indicates the number of atoms involved in the deformation process. It can be estimated using the usual equation [86]:

$$mVH = 3\sqrt{3}kT \tag{3-24}$$

where m is SRS value (=1/n) and other parameters have their usually meanings. By inserting values for each variable into equation (3-24), the activation volumes are calculated and listed in Table 3.1 as shown in section 3.2. The activation volume appears to be insensitive to the indentation load and decreases only slightly with increasing temperature. It has a value of about 2.5-3.5b^3 and is noted to be only half of the value reported for nc-Ni measured at room temperature [87]. The lower activation volume may be caused by thermal relaxation at elevated temperatures. Thereby, additional effort was made to perform stress relaxation tests on the nc-Ni to measure the activation volume at ambient temperature. The result is shown in Figure 3.6. It is evident that, even at ambient temperature in a time duration of 30 seconds, a significant drop of ~ 350MPa is recorded. The activation volume can be extracted from the equation [88]:

$$\Delta\tau = -\frac{kT\ln(1 + t/t_r)}{V} \tag{3-25}$$

where t is the time, t_r is the characteristic relaxation time, and $\Delta\tau$ is the decay of stress during the stress relaxation process. By fitting the curve, V is calculated to be 3.33b^3, which is only slightly higher than the high temperature values listed in Table 3.1. Therefore, temperature appears to be not the major factor for the recorded small activation volume in the current study.

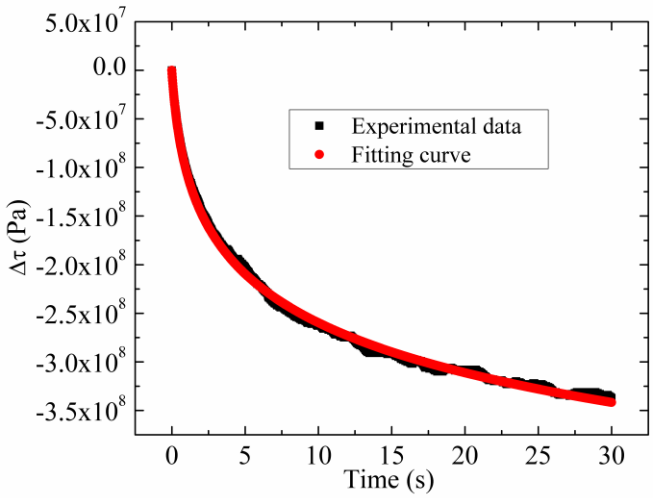

Figure 3.6 Stress relaxation as a function of time for nc-Ni at ambient temperature.

3.6 Microstructure

Microstructure of the as-deposited Ni specimen was observed using TEM, a representative image is shown in Figure 3.7, which consists of grains with large misorientations [69]. As the grain structure in nc-Ni is known to be unsTable at high temperatures [89-91], thermal annealing on the as-deposited nc-Ni performed at the test temperatures for 1800 seconds (i.e. the holding time prior to creep testing in the current study). There was significant grain growth and the average grain sizes of the samples annealed at 348, 398 and 448 K are 47, 60 and 77 nm, respectively. These annealed grain sizes were noted to be the starting grain size in the current nanoindentation study.

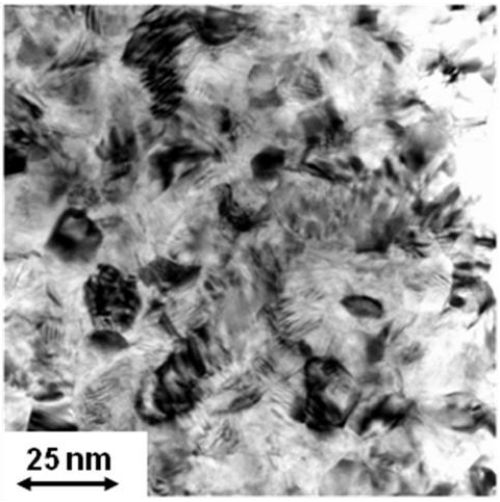

Figure 3.7 Bright-field TEM image of the as-deposited Ni, showing the averaged grain size is about 14 nm. The majority of grain boundaries is high-angled.

Zhang et al [92] have reported a rapid stress-driven grain growth in nc-Cu at both room and cryogenic temperatures. This dynamic grain growth was also observed during the indentation of a commercial nc-Ni (Integran Inc.) at low strain rates [65]. In contrast, Brandstetter et al [93] reported no coarsening was observed in electrodeposited nc-Ni under both compression and indentation tests at room temperature. Thus, we made efforts to examine the microstructure of a crept sample. A thin film TEM sample extracted and lifted from the bulk sample of nc-Ni crept at 448 K under a load of 9 mN is presented in Figure 3.8, and its corresponding cross-section bright field STEM image is shown in Figure 3.9. The average size of the nc grains is about 77 nm with a size distribution ranging from 60 nm to 170 nm. The average grain size is the same as the starting value measured by XRD technique. Furthermore, it is noted in Figure 3.9 that grain structures in

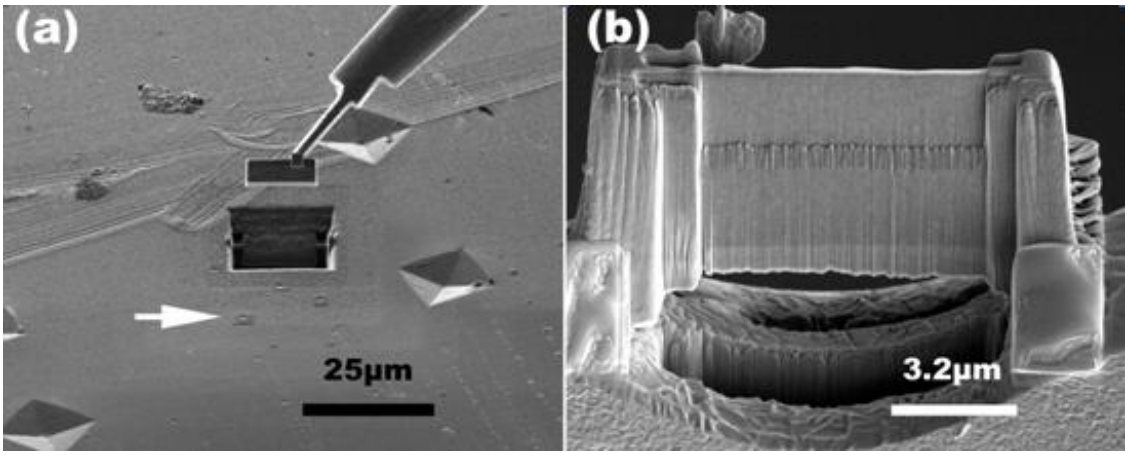

Figure 3. 8 (a) Ion-beam image showing the in-situ lift-out of a TEM cross-section sample by Omniprobe AutoProbe; (b) A typical STEM image of the completed cross-section TEM specimen after the final thinning. (Courtesy of Dr. M. Zhang)

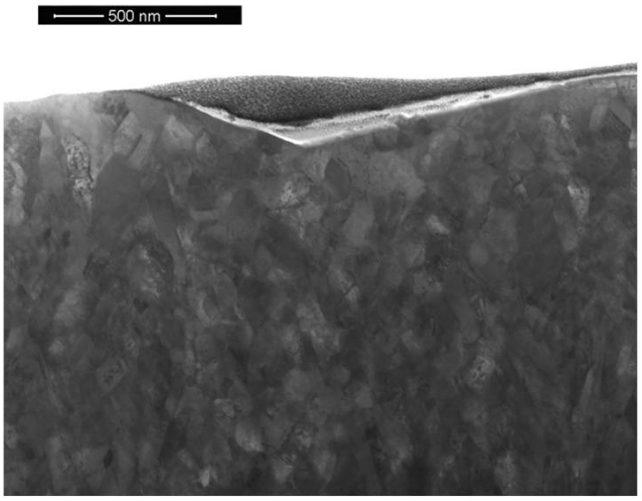

Figure 3.9 Bright-field STEM image of Ni indent crept at 448 K and load of 9 mN, showing the grain structure is uniform and the average size is about 77 nm.

the regions right underneath and far from the indentation are not much different, which indicates there is no dynamic grain growth.

3.7 Discussion of the Deformation Mechanisms

It is always appealing to invoke grain size dependent mechanisms such as diffusional creep or grain boundary sliding as the deformation process in nc-materials. For example, Yin et al [28] and Wang et al [22] performed uniaxial tension creep with nc-Ni and concluded that the deformation was controlled by a Coble-type diffusional mechanism. In the current nc-Ni, however, the mechanism is not likely to be a diffusional creep-type since the stress exponent is far from unity. Therefore, diffusional creep cannot play a major role in the current nc-Ni.

Another intuitive expectation for mechanism is grain boundary sliding, since the presence of significant grain boundary area in nc-Ni can readily facilitate the sliding process. A direct evidence of grain boundary sliding in nc-materials is difficult to obtain because the lack of any "inertial marker". However, even grain boundary sliding might have occurred in the current nc-Ni, the following arguments can exclude it as the dominant deformation process.

It is recognized that internal friction technique can be used to determine the optimum temperature for superplasticity, thus grain boundary sliding, in fine-grained materials [94]. The peak of internal friction, which corresponds to the optimum temperature for superplasticity, usually shifts to a lower temperature as the grain size is reduced. For instance, peaks for Mg alloys with a grain size of 0.8 and 1 μm occur at 533 and 573 K, respectively. These two temperatures are also for the maximum superplastic

elongation (or maximum grain boundary sliding). For superplasticity that is controlled by grain boundary diffusion it can be described by the equation [95]:

$$\dot{\varepsilon} = A(\frac{b}{d})^3(\frac{\sigma}{E})^2 \exp(-\frac{Q_{gb}}{RT}) \tag{3-26}$$

where d is the grain size, A is a material constant, $\dot{\varepsilon}$, σ, b, E and Q_{gb} have their usual meanings.

Internal friction measurement is usually performed at a fixed frequency, which corresponds to $\dot{\varepsilon}$ = constant. During constant stress creep we have a simplified equation:

$$d^{-3}\exp(-\frac{Q_{gb}}{RT}) = constant \tag{3-27}$$

Using Q_{gb}(Mg) = 92 kJ/mol, the peak position of internal friction (or temperature for the maximum grain boundary sliding) in Mg with a grain size of 50 nm would be approximately 365 K (92 ℃), which corresponds to 0.40 T_m, where T_m is the absolute melting point of Mg. For Ni, 0.40 T_m would be about 690 K (or ~ 417 ℃). Interestingly, nc-Ni has been shown to exhibit superplasticity at a temperature as low as 350 ℃ (~ 0.36 T_m) [96]. 350 ℃ might be considered low for superplastic Ni, but is higher than the highest temperature used in the current study (175 ℃). Based on the above estimation, grain boundary sliding may have some contributions but is certainly not the dominant one.

As summarized in results, nanoindentation creep of nc-Ni at elevated temperatures (348-448 K) showed a stress exponent about 3-10, activation energy close to that for the grain boundary diffusion, a relatively small activation volume. From these results, it appears tempting to suggest that power-law creep might be the dominant mechanism. This

is because equation of power-law-type has often been used for data analysis of indentation creep [45, 49, 56]. However, it is necessary to point out that power-law analysis is an empirical approach mainly for the convenience of mathematical treatment. A good fitting of data does not necessarily imply the physical mechanism is dislocation climb or glide.

Nanoindentation creep rate reported in the literature is notably faster than about 10^{-3} s^{-1}. In contrast, uniaxial creep rates for alloys are typically less than 10^{-4} s^{-1} [95]. The higher strain rate reported for nanoindentation creep is a result of the fact that test time is normally less than 100-1000 s. The short testing time is to minimize thermal drift and electronic instability of the nanoindentation unit. This is an intrinsic limitation or drawback of measuring nanoindentation creep. A strain rate of 10^{-3} s^{-1} is actually in the same range as that for conventional tension/compression. To further clarify this point, we plot the temperature-compensated creep rate data as a function of stress in a double-logarithm graph, as shown in Figure 3.10. Also included in this Figure are uniaxial creep data for sub-micro-sized and nc-Ni previously reported in several papers [28, 35, 97]. To make a direct and fair comparison, the current nanoindentation creep data in Figure 3.10 were actually the converted data of equivalent uniaxial strain rates via the equation:

$$\dot{\varepsilon}_u = \beta \bullet \dot{\varepsilon}_I \tag{3-28}$$

where the constant $\beta \approx 0.09$ [56]. All the creep data in Figure 3.10 are noted to follow a consistent trend, namely, the low stress data obey a power-law ($n = 3$) and gradually transit to a region with much steeper slope, i.e. high stress exponent. It is evident in the Figure that current nanoindentation data and data from Kottada et al [35] are in the high stress (or strain rate) region, where the creep rate increases more rapidly than any power of

stress, or has an extremely high "apparent" stress exponent. Gu et al [87] also reported the n value as high as 30 during nanoindentation. This is the region known as the power-law breakdown region. In this region, creep data are typically subject to large variations because of the strong stress dependence. The mechanism for power-law breakdown is poorly known but has been proposed to be a result of substructure rearrangements, e.g., subgrain or cell formation [98]. However, such a mechanism is not expected to operate in the current nc-Ni since the grain size is much smaller than the dimension of subgrain or cell in Ni, which is estimated to be about 200 nm [35]. Our TEM image of the deformed sample also confirms the absence of subgrain or cell formation (Figure 3.9).

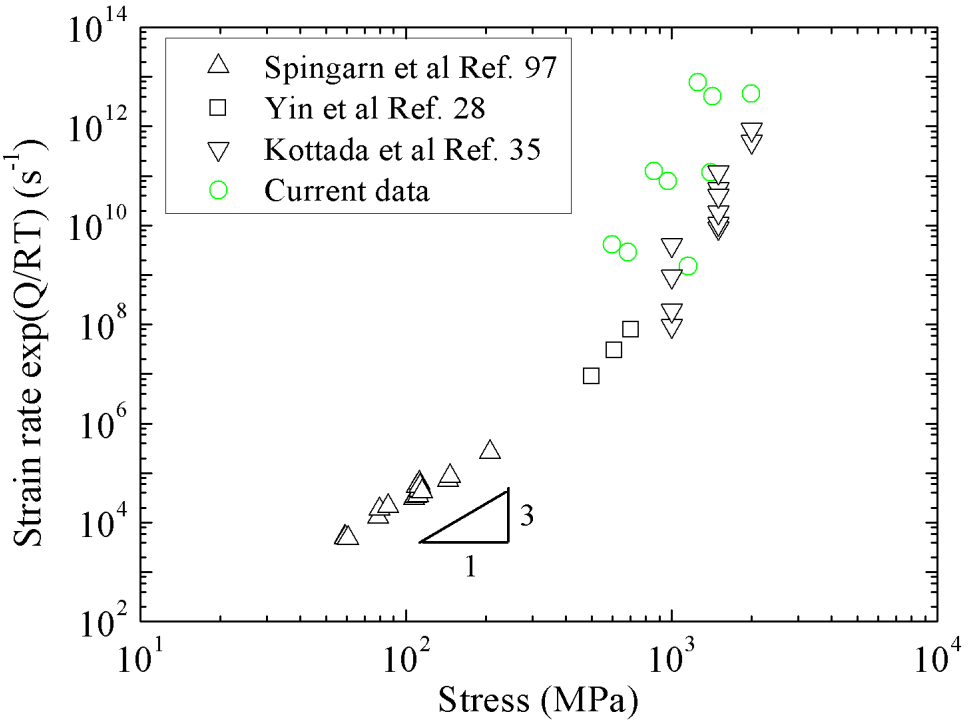

Figure 3. 10 Log-log plot of temperature compensated creep rate versus stress for the Ni. Creep data of nc-Ni from other sources [28, 35, 97] are included for comparison.

Despite the exact mechanism is still unclear, the activation energy measurement indicates that grain boundary diffusion controls the recovery process. The intergranular self-diffusion coefficient of nc-Ni is about 10^{-18} m^2 s^{-1} at 373 K. At the test temperatures range from 348 to 448 K, the traveling distance of atoms is estimated to be in the order of 10 nm along intergranular boundaries in the duration of indentation, which is about 28 lattice spacings for Ni, sufficiently long to locally accommodate deformation processes such as grain boundary sliding, grain migration, and grain rotation. This confined atom transport along grain boundaries may also explain the relatively low activation volume obtained in the present study.

3.8 Conclusions

Nanoindentation creep behavior of nanocrystalline Ni with the as-deposited grain size of 14 nm under fixed loads of 1, 5 and 9 mN, and temperatures ranging from 348 to 448 K were investigated. The following observations are made.

1. Based on a power-law-type analysis, the creep stress exponent ranged from 3 to 10 and generally decreased with increasing temperature and applied load. The thermal drift rate effect on the measurement of stress exponent was typically about 5%.

2. The creep activation energy was about 123 kJ/mol, which was close to that for the grain boundary self-diffusion. This result indicated that grain boundary diffusion controlled the recovery process.

3. A relatively small activation volume of about 2.5-3.5b^3 was obtained, which was probably due to the fact that the deformation took place primarily within the confined grain boundary region.

4. Diffusional and grain boundary sliding processes were ruled out as the dominant deformation mechanisms during nanoindentation creep of the current nc-Ni.

5. A power-law-type equation appeared to be a convenient way to describe the nanoindentation creep behavior of nc-Ni. However, a direct comparison with the exiting literature data indicated the stress (or strain rate) level was too high to be in the power-law creep regime (i.e. controlled by dislocation climb or glide). In fact, the current nanoindentation creep data fall in the power-law breakdown regime.

Chapter 4 Uniaxial Creep of nc-Nickel and its Direct Comparison with Nanoindentation Creep

This chapter is a slightly revised version of a paper entitled "Creep of nanocrystalline nickel: A direct comparison between uniaxial and nanoindentation creep" published in *Scripta Materialia* in 2010:

C. L. Wang, Y. H. Lai, J. C. Huang and T. G. Nieh, Creep of nanocrystalline nickel: A direct comparison between uniaxial and nanoindentation creep", *ScriptaMaterialia* 62 (2010) 175-178.

My primary contributions to this paper include (1) most of the experiment work, (2) most of the data analysis, (3) most of the writing.

Creep behavior of nc-Ni have been successfully characterized by nanoindentation technique as described in chapter 3. Nanoindentation creep has been demonstrated to be an effective and convenient way to study creep behavior of materials, especially materials with limited volume. To take a full advantage of nanoindentation technique to study the creep behavior of the materials, corresponding uniaxial data need to be generated and compared. For this purpose, the uniaxial creep data were obtained by performing microcompression creep tests on micropillars. The uniaxial compressive creeps were conducted at peak loads range from 3.6 to 5 mN at 398 K. The loading and unloading time was set to be 1 s and a peak load holding duration of 60 s was set in the loading function. The morphology of pillars before and after deformation was examined by SEM. The data

obtained from uniaxial creep were directly compared with that from nanoindentation creep at the same temperature.

4.1 Results from Uniaxial Creep of nc-Nickel

Typical SEM micrographs of pillar before and after creep at a fixed load of 5 mN are shown in Figure 4.1. It is noted from Figure 4.1(a) that the sidewall of pillar is not parallel to its axis, but has a taper angle of about 3^o with respect to the test axis. This is an inherent byproduct of the current FIB technique. This taper effect was taken into account when analyzing stress and strain in the pillars by adoption of a fixed taper angle of 3^o and conservation of volume during deformation. One apparent feature of the deformed pillars is the uniform deformation, as shown in Figure 4.1(b). In general, all crept pillar samples were uniformly deformed in contrast to inhomogeneous, localized slips observed in single crystalline materials [74].

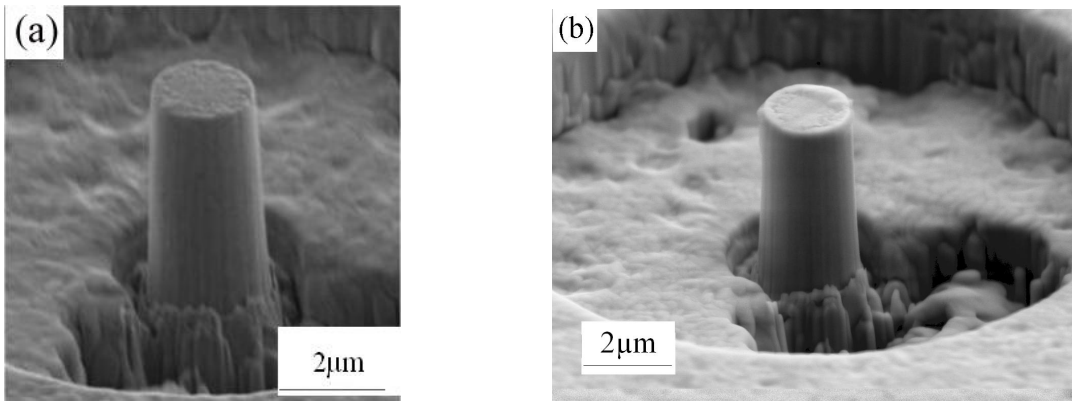

Figure 4.1 SEM micrographs of the Ni14 pillar crept at a fixed load of 5 mN (a) before and (b) after creep.

The load and displacement recorded during uniaxial creep were converted into true stress and true strain by assuming a constant taper angle of 3 °during creep. The uniaxial strain rate $\dot{\varepsilon}_u$ under uniaxial creep was calculated using the equation:

$$\dot{\varepsilon}_u = \frac{d\varepsilon}{dt} = \frac{dl}{ldt} \tag{4-1}$$

where ε is true strain, t is time and l is instantaneous length of the pillar.

The strain-time plots for pillars crept under different loads are shown in Figure 4.2. It can be readily observed that strain initially increases sharply with time, followed by a decreasing strain rate, and then exhibits steady-state type behavior, i.e. the strain increases linearly with time.

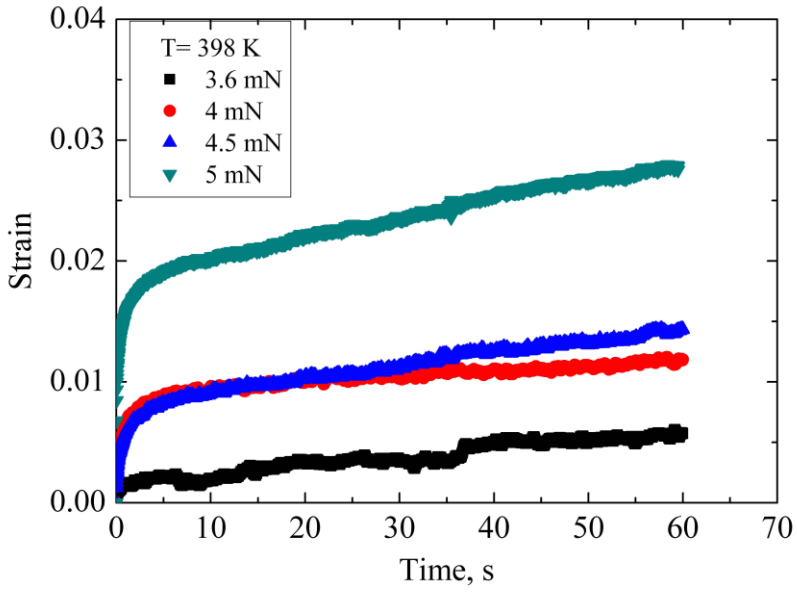

Figure 4.2 True strain-time curves for Ni14 crept at 398 K and different loads as indicated on the plot.

In the uniaxial creep tests, constant loads were applied and the stress level at the end of each test was less than 1% lower than the stress at the beginning of the creep. Thus, it is essentially a constant stress creep condition. The uniaxial steady-state creep rate $\dot{\varepsilon}_u$ versus stress relationship plotted in a double-logarithmic graph is given in Figure 4.3. The stress exponent value, i.e. the slop of the fitting curve, is about 5.13 as indicated on the Figure.

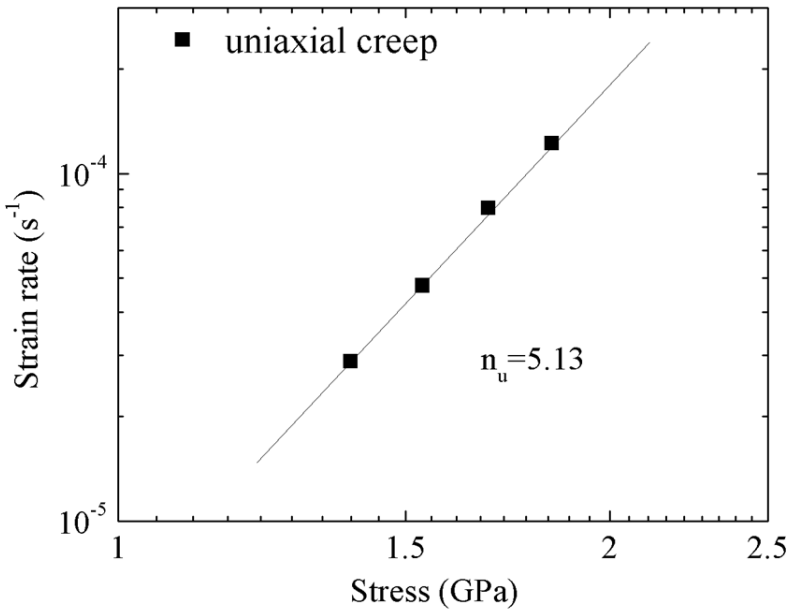

Figure 4.3 Strain rate versus stress for uniaxial creep of Ni14.

4.2 Direct Comparison of Nanoindentation and Uniaxial Creep

4.2.1 Direct Comparison of Results from Nanoindentation and Uniaxial Creep

In order to ascertain the correlation between the data from nanoindentation creep and that from uniaxial creep, especially the correlation coefficient β, i.e. ratio of uniaxial creep rate $\dot{\varepsilon}_u$ and indentation creep rate $\dot{\varepsilon}_I$, a direct comparison of the two set of data was made. The stress and strain rate data obtained under two kind of tests conducted at the same temperature of 398 K are plotted in Figure 4.4. It need to pointed out that, in this Figure, the applied stresses under nanoindentation are computed through the classical Tabor relationship: $H = \alpha\sigma$, $\alpha = 3$[39], although there are indications that α may be less than 3 at high temperatures [99].

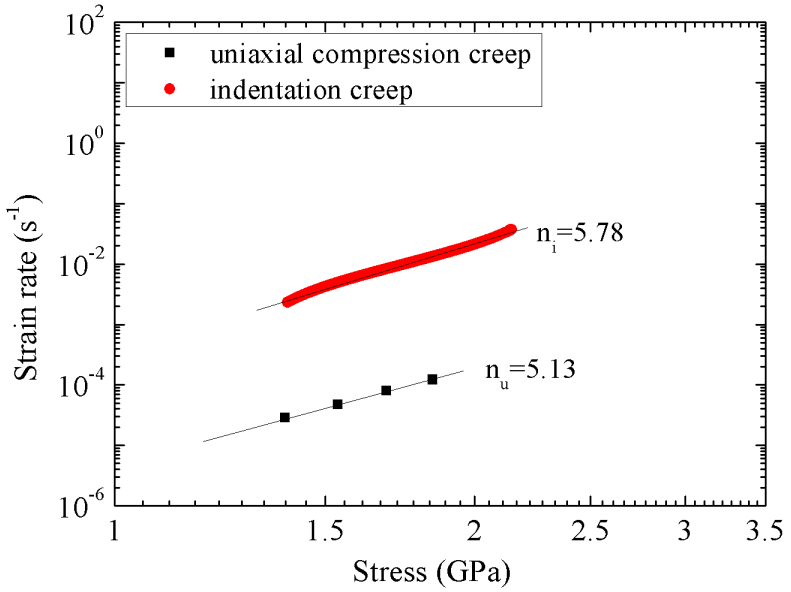

Figure 4.4 Plot of strain rate as a function of stress from uniaxial creep and nanoindentation creep.

It is evident in Figure 4.4 that the nanoindentation creep follows a power-law with a stress exponent, n_I, of about 5.78, which is almost the same as n_u (=5.13) obtained from the uniaxial creep. This result is similar to that reported in polycrystalline indium, in which both n_I and n_u are essentially identical (≈ 5) [45]. The fact that the stress exponent is almost identical under the two creep conditions is somewhat expected since the underpinned creep mechanism in both cases is the same. The temperature dependence (i.e. the creep activation energy) for the two creeps is also the same. As shown in section 3.4, the activation energy corresponds to that for grain-boundary diffusion in Ni, suggesting that both cases are dislocation climb creep with the rate controlling step to be grain boundary diffusion. The only difference between the two creeps appears to be the magnitude of creep rate. Strain rates at different stress levels for the two creeps are listed in Table 4.1. At a fixed stress, the nanoindentation creep rate is noted to be much faster than the uniaxial creep rate. Specifically, the ratio of the two creep rates ($\dot{\varepsilon}_u / \dot{\varepsilon}_I$) is about 0.01 for the current nc-Ni. In comparison, the ratio was only about 0.09 for amorphous Se. In other words, β (≈ 0.01) for nc-Ni appears to be about 1/10th of that for amorphous Se ($\beta \approx 0.09$). The difference will be rationalized in section 4.2.2.

Table 4.1 Stress or (Hardness/α), strain rate, and strain rate ratio under uniaxial and nanoindentation creep at 398 K.

Stress or (Hardness/α), GPa	Strain rate, s^{-1}		Strain rate ratio, $\dot{\varepsilon}_u / \dot{\varepsilon}_I$
	Uniaxial creep, $\dot{\varepsilon}_u$	Nanoindentation creep, $\dot{\varepsilon}_I$	
1.388	2.88×10^{-5}	2.5×10^{-3}	11.5×10^{-3}
1.53654	4.75×10^{-5}	4.93×10^{-3}	9.63×10^{-3}
1.68637	7.96×10^{-5}	8.30×10^{-3}	9.59×10^{-3}
1.84433	1.22×10^{-4}	1.32×10^{-2}	9.24×10^{-3}

4.2.2 Discussion of the Reasons for the Difference Observed in Nanoindentation and Uniaxial Creep

A uniaxial mechanical test monitors the response of a material under a relatively uniform stress state in a global way. By contrast, nanoindentation probes the material response from a local volume. In addition, stress state under an indentation, which depends on the intrinsic properties of a material, is complex and is actually much more severe than that under the uniaxial condition. To the first approximation, it can be viewed as biaxial stress state. It has been demonstrated [100] that, at the same equivalent stress, deformation rate under biaxial condition is faster than that under uniaxial. Therefore, a faster nanoindentation creep rate as compared to uniaxial creep rate in Se is somewhat anticipated, at least qualitatively. In the current case of nc-Ni, however, the gap between the two creep rates is much larger.

It is noted that, to evaluate the nanoindentation creep rate, α =3 is commonly applied in the Tabor relation: $H = \alpha\sigma$. At high temperatures, however, α would be expected to be lower because of a reduced strain hardening and enhanced thermal recovery. In the description of nanoindentation creep, the power-law equation can be written as

$$\dot{\varepsilon}_I = A^{'}\sigma^n = A^{'}(\frac{H}{\alpha})^n \tag{4-2}$$

In this equation, the strain rate is inversely proportional to the Tabor factor α to the *n*th power. In the case of amorphous Se, which flows in a Newtonian fashion ($n = 1$), a variation of α can only affect the actual creep rate in a linear and insignificant manner. By contrast, nc-Ni has a stress exponent of about 5, the selection of α can shift the actual creep rate in a much dramatic way.

Only limited parallel hardness-strength data as a function of temperature are available in the literature [99, 101]. In the case of a Zr-2.5Nb alloy [99], in particular, it was found that the Tabor factor decreases as the temperature increases, and $\alpha \approx 2.09$ at 0.27 T_m, where T_m is the melting temperature of the alloy. This homologous temperature is, in fact, similar to the creep temperature of 0.23 T_m used in the current study of nc-Ni. A selection of 2 instead of 3 for the Tabor factor can change the nanoindentation creep rate by a factor of over 8 (leading to $\beta \approx 0.08$), which is reasonably accounTable for the observed difference in the β ($= \dot{\varepsilon}_u / \dot{\varepsilon}_I$) value between Se and nc-Ni. The nanoindentation creep rate versus hardness compensated by various Tabor factors is presented in Figure 4.5.

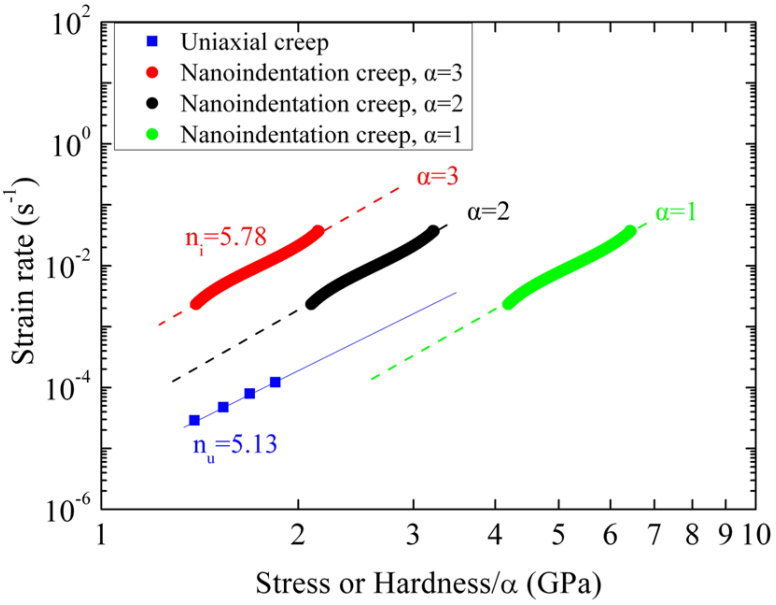

Figure 4.5 Strain rate versus stress or hardness compensated by different α for nc-Ni from uniaxial creep and nanoindentation creep, respectively.

Three important points deserve further discussion. The first one is the creep mechanism, in particular, during nanoindentation. As pointed out in section 3.7 that several independent mechanisms: diffusional creep, grain boundary sliding and power-law creep might operate concurrently during nanoindentation. However, diffusional creep or grain boundary sliding was ruled out as the dominant mechanism, even they both might occur. Two main factors support this conclusion. First, the test temperature was 398 K (125 ℃), which is only about $0.23T_m$. Diffusional creep and grain boundary sliding mechanisms dominate typically around 0.7 T_m and above. For nc-Ni this temperature may

be lower but is unlikely to be as low as 0.23 T_m. Second, assuming the three mechanisms are operating independently, the total creep rate $\dot{\varepsilon}_{total}$ can be estimated approximately by

$$\dot{\varepsilon}_{total} = v_d \dot{\varepsilon}_d + v_{gbs} \dot{\varepsilon}_{gbs} + v_p \dot{\varepsilon}_p \tag{4-3}$$

where $\dot{\varepsilon}_d$, $\dot{\varepsilon}_{gbs}$, and $\dot{\varepsilon}_p$ represent the creep rates caused by diffusional creep, grain boundary sliding, and power-law creep, respectively, v_d, v_{gbs}, and v_p represent the corresponding weighted volume fraction of region affected by each creep, and $v_d + v_{gbs} + v_p = 1$. The exact values of v_d, v_{gbs}, and v_p are determined by applied stress, temperature and properties of Ni, but they are probably within one order of magnitude. On the other hand, $\dot{\varepsilon}_d$, $\dot{\varepsilon}_{gbs}$, and $\dot{\varepsilon}_p$ depend upon the applied stress raised to a power of 1, 2, and 5, respectively. Obviously, $\dot{\varepsilon}_p$ has the strongest stress dependence. This, together with the fact that the test temperature is only $0.23 T_m$, leads nc-Ni favors the power-law creep, even the grain size is small.

The second important point is the pillar sample damage by FIB process. One may argue that the creep rate difference is a result of sample surface contamination by Ga ion. However, it is noted that the penetration depth for 30 keV Ga ion (i.e. the energy used for the current processing of Ni pillar) in Ni is only 10-20 nm [102]. Comparing with the diameter of the pillar ~ 2000 nm, it is relatively small. Specifically, taking the penetration depth 20 nm, the ratio of Ga ion affected cross sectional area is only about 4% of the total cross sectional area of the pillar. In this case, the unaffected region is dominating the overall behavior of the pillar.

The last question is possible surface oxidation during indentation. Ni does not exhibit noticeable oxidation until T > 400-500˚C [103], which is much higher than the current test temperature of 125 ˚C. Thus, oxidation is expected to be negligible. In fact, nc-Ni samples look still shining after testing.

4.3 Conclusions

Uniaxial creep was conducted on nanocrystalline nickel with an as-deposited grain size of 14 nm at 398 K and loads from 3.6 to 5 mN. The results were directly compared with that obtained from the same material deformed at the same temperature but under nanoindentation creep. The following observations are made.

1. Uniaxial creep is found to have a stress exponent of 5.13, which is similar to that observed under nanoindentation creep. These two creeps are expected to have a similar stress exponent because the underpinned deformation mechanism is the same.

2. The creep rate under nanoindentation is typically much faster than that under uniaxial creep. The faster creep rate was caused by the facts that the stress state under nanoindentation is more complex and severe than uniaxial condition, and the conversion factor used from hardness to stress (i.e. the Tabor factor) is less than the typical value of 3. In fact, in the current case of nc-Ni, after replacing with a proper Tabor factor, the difference between the two creeps can be brought into reasonable agreement in line with that previously observed in amorphous Se.

Chapter 5 Mechanical Hysteresis and Grain Boundary Sliding in Nanocrystalline Nickel

It is generally recognized that dislocation-mitigated process is limited during plastic deformation of nc-metals with a grain size less than about 50 nm. As a result of extremely small grains, nc-metals have a high volume fraction of grain boundaries. Plastic deformation in nc-metals is, therefore, mainly controlled by facile grain-boundary processes such as grain boundary sliding, migration and rotation, and cooperative shear. High energy grain boundaries are expected to facilitate sliding when they are under shear.

Up to now, the interrupted deformation characteristics of nc-materials has not received much attention. Such information is important for accessing the viability of nc-materials in structural applications, where repeated loading occurs. In the current study, the multiple interrupted unload-reload tests were conducted on electrodeposited nc-Ni in both tension and compression. The tests were conducted under a displacement control mode with nominal strain rates of 5×10^{-4}, 10^{-3} and 10^{-2} s^{-1}. For compression, the unloading of each cycle was carefully controlled such that the punch always making intimate contact with the top surface of the pillar. For cyclic unload-reload in tension, the samples were loaded to preset displacement with equal increment between two cycles. For the unloading segment of each cycle, the stress was reduced to 20 MPa except for the last cycle to zero. There was no holding time between each unloading segment and its following reloading segment for both tension and compression tests.

5.1 Results from Unload-Reload Tests of nc-Nickel

The true stress-strain curve for Ni65 pillar compressed at a strain rate of 10^{-3} s^{-1} with six unload-reload interruptions is shown in Figure 5.1. It is evident that in each unload-reload cycle, the reloading curve does not trace exactly the unloading curve and produces a hysteresis loop. For clarity and to reveal the hysteresis clearly, loops 2, 4 and 6 are magnified and replotted in the lower part of Figure 5.1. These hysteresis loops represent irreversible energy dissipation. The amount of energy can be estimated from the size of loop, i.e.

$$\Delta E = \oint \sigma \, d\varepsilon \tag{5-1}$$

where ΔE is the energy per unit volume. As indicated in Figure 5.1 that the size of loop increases as deformation proceeds. At other strain rates, for example, 5×10^{-4} and 10^{-2} s^{-1}, the stress-strain curves of Ni65 exhibit a similar trend, i.e. the size of hysteresis loop enlarges as the compressive strain increases. Although not shown here, compressive stress-strain curves of Ni43 with several interrupted unload-reload cycles reveal a similar phenomenon. In the case of tension at various strain rates, Ni43 and Ni65 also behave in a similar fashion, the loop size increases with the deformation strain.

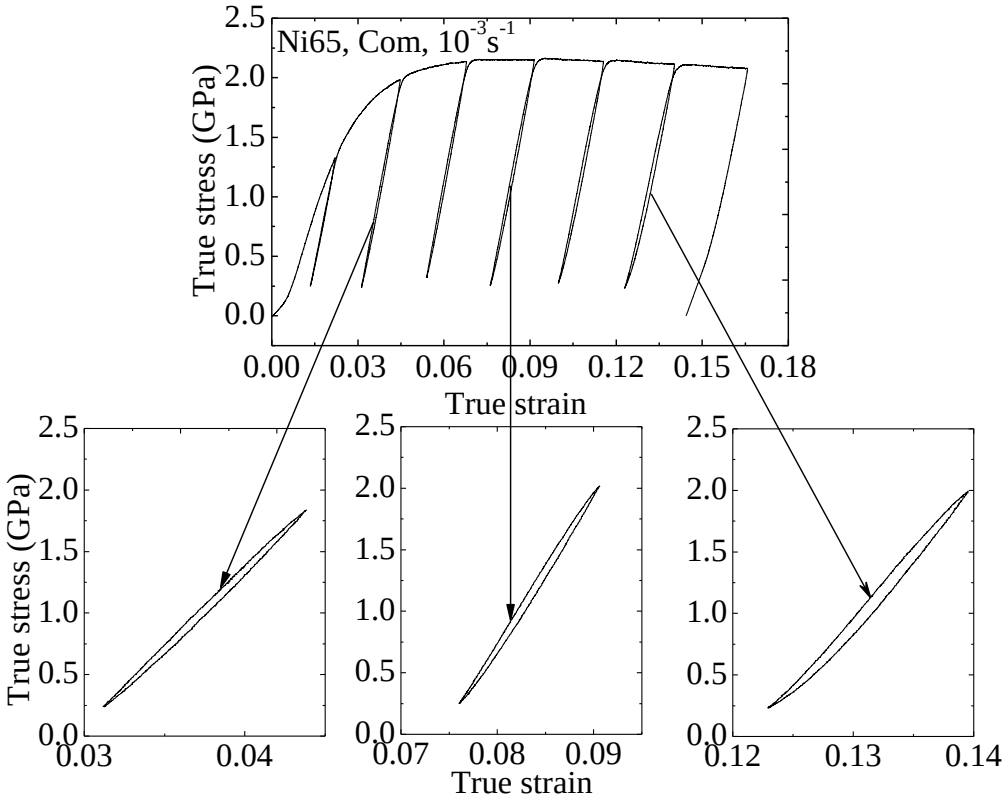

Figure 5.1 True stress versus true strain curve for Ni65 pillar deformed at a strain rate of 10^{-3} s^{-1}. Hysteresis loop from the second, fourth and sixth unload-reload cycles are enlarged for clarity.

5.2 Grain Boundary Sliding Model

Since dislocation activity is limited during plastic deformation in nc-metals, especially at a grain size less than about 50 nm [12, 104], the observed hysteresis is, therefore, expected to be primarily resulted from grain boundary sliding, which is usually the dominant deformation process in fine-grained materials. To demonstrate this is the case and for the simplicity of arguments, let us assume grains are arranged as columnar

hexagons with side length D, as indicated in Figure 5.2. The length of the grain column is l. Also for the simplicity of illustration, only two grains are shown. Under an applied stress σ, the two neighboring grains slide upon each other by a small distance of λ, as indicated in Figure 5.2(b). The sliding is caused by a shear stress τ, where $\tau = \sigma \sin\theta$ and θ is the angle between the applied stress σ and the boundary. Upon sliding, work W_i is done by the shear stress on this particular boundary plane which can be expressed by the following equation:

$$W_i = \tau l D\lambda = D\sigma l\lambda \sin\theta_i \tag{5-2}$$

The total work W_{total} done by the applied stress is, then, the summation of the local work W_i from n individual grain boundaries, i.e.

$$W_{total} = \sum_i^n W_i = \sum_i^n D\sigma l\lambda \sin(\theta_i) = \frac{1}{\pi}\int_0^\pi [D\sigma l\lambda \sin(\theta)]d\theta = (2D\sigma l\lambda)/\pi \tag{5-3}$$

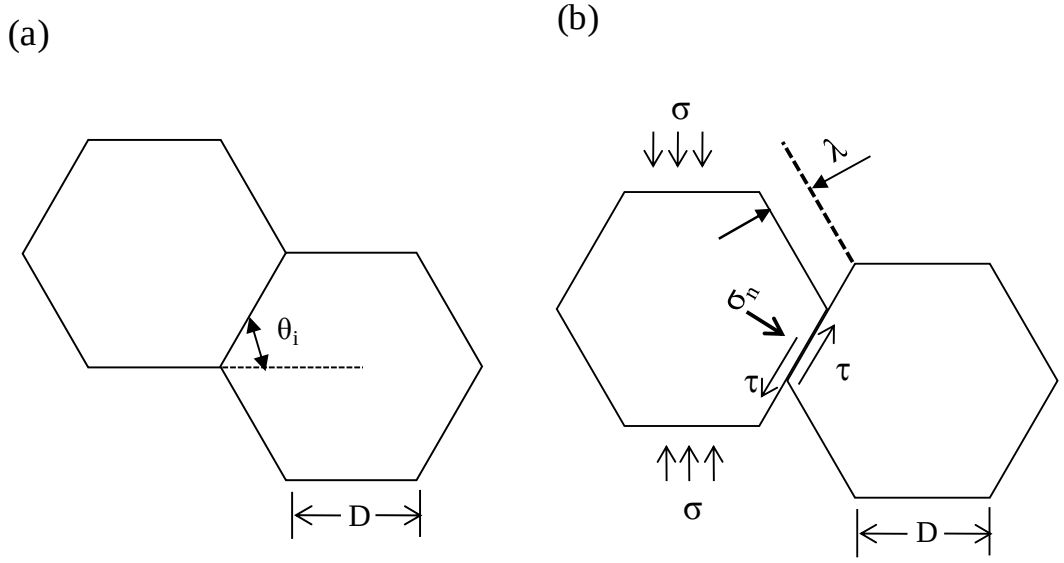

Figure 5. 2 Schematic illustration of two neighboring grains (a) before and (b) after sliding.

In the case of having perfect hexagons, $\theta_i = 60^\circ$. The volume of the test sample, V, scales with the average volume of grains, thus, $V = \alpha l D^2$ where α is a geometric constant. Combining equations (5-1) and (5-3), we obtain

$$\Delta E = \frac{W_{total}}{V} = \frac{2\sigma\lambda}{\pi\alpha D} = \alpha'\sigma(\frac{\lambda}{D}) = \alpha'\sigma\varepsilon_{gbs} \tag{5-4}$$

where $\alpha' = 2/\pi\alpha$ is a constant and ε_{gbs} is the sliding strain. For grain boundary sliding, the grain boundary sliding rate $\dot{\varepsilon}_{gbs}$ can be expressed by the following equation [95]:

$$\dot{\varepsilon}_{gbs} = \frac{B\sigma^2}{d^p}\exp(-\frac{Q}{RT}) \tag{5-5}$$

where B is a parameter depends on the material, Q is the activation energy, RT has its usual meaning, d is the grain size, and p is the grain size exponent (p =2 or 3, when sliding is controlled by lattice diffusion or grain boundary diffusion, respectively).

The sliding strain, ε_{gbs}, is expected to scale with the total plastic strain, i.e. $\varepsilon_{gbs} = \beta\varepsilon_{total}$. This leads to the sliding rate $\dot{\varepsilon}_{gbs} = \beta\dot{\varepsilon}_{total}$, where β is a scaling factor. In either uniaxial compression or tension, which is typically at a fixed strain rate and temperature, the sliding strain is

$$\varepsilon_{gbs} = \int_0^{\Delta t} \dot{\varepsilon}_{gbs}\,dt = \dot{\varepsilon}_{gbs}\Delta t = \frac{B\sigma^2\Delta t}{d^p}\exp(-\frac{Q}{RT}) = B'\frac{\sigma^2\Delta t}{d^p} \tag{5-6}$$

where B' is a constant and Δt is the sliding time. Insert this into equation (5-4), we have

$$\Delta E = \frac{W_{total}}{V} = \frac{2\sigma\lambda}{\pi\alpha D} = \alpha'\sigma(\frac{\lambda}{D}) = \alpha'\sigma\varepsilon_{gbs} = A\frac{\sigma^3\Delta t}{d^p}$$

or

$$\frac{\Delta E}{\Delta t} = \dot{E} = A\frac{\sigma^3}{d^p} \tag{5-7}$$

This equation indicates the energy dissipation rate, $\dot{E}$, should scale with the applied stress raised to a third power at a fixed grain size and temperature.

5.3 Discussion

The energy dissipation rate computed from the size of each loop and its corresponding dissipation time. The rate data as a function of stress from both compression and tension are displayed in Figure 5.3 for Ni65 at different strain rates. It is readily observed that the energy dissipation rate increases with stress. Furthermore, all data fall on a line with a slope of approximate 3 for each strain rate, especially at low stresses, supporting the idea that the deformation process is indeed dominated by grain boundary sliding, as predicted by equation (5-7). Another worth noting feature in Figure 5.3 is that the energy dissipated in tension is slightly higher than that in compression. It is probably caused by the fact that nc-metals exhibit strength asymmetry [105-106], i.e. the tensile yield strength is lower than that of compression. The strength asymmetry suggests shear in nc-metals is pressure-dependent, and in particular, affected by the normal stress on the slip plane. Thus, grain boundary is relatively easy to slide under tension than compression at the same applied stress level.

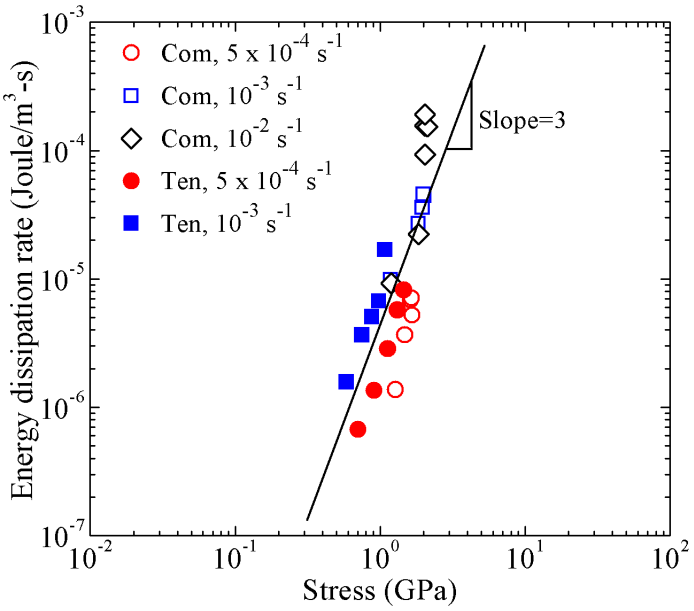

Figure 5.3 Energy dissipation rate as a function of stress for Ni65 under both compression and tension at various strain rates. Hollow and solid symbols represent data collected in compression and tension, respectively.

According to equation (5-7) the energy dissipation rate is also expected to increases as the grain size decreases. Therefore, efforts were made to evaluate the hysteresis during unload-reload in Ni43 samples in tension and the results are presented in Figure 5.4. Data from Ni65 are also included in the Figure for a direct comparison. It is observed that $\dot{E}$ for Ni43 is also proportional to the flow stress raised to the third power. In addition, $\dot{E}$ from Ni43 is noted to be slightly higher than that from Ni65, especially at the lower strain rate. In fact, equation (5-7) would predict an increase of 2-3 times in $\dot{E}$ for Ni43 as

compared to Ni65. The exact amount is dependent upon the p value (or the controlling diffusion mechanism).

One note is about possible boundary relaxation during unload-reload cycle. Based on the model proposed by Schneibel and Hazzledine [107], the relaxation time is proportional to the grain size raised to the fourth power and is estimated to be 9344 and 48700 s for Ni with a grain size of 43 and 65 nm, respectively. The data employed in the calculation are T =298 K, grain boundary thickness δ =1 nm, D_{gb} =2.7 x 10^{-18} m^2s^{-1} [108], Ω =8.08 $\times 10^{-30}$ m^3, and γ =0.98 J/m^2 [109]. The slowest strain rate used in the present study was 5 $\times 10^{-4}$ s^{-1} and the unloading time is in the range of 9-67s, which is far less than the relaxation time. Therefore, anelastic recovery during unloading is considered negligible and the strain is essentially from plastic deformation (i.e. grain boundary sliding). Another note is the possible grain growth during deformation of nc-Ni at room temperature [65, 110]. We conducted TEM examinations of the microstructure both before and after deformation. The majority of grains in the materials prior to deformation was high-angled and remained so after deformation. In the case of Ni43, in particular, the starting mean grain size was 43 nm and grew slightly to 48 nm after plastic deformation. This consistent with the literature that grain growth of nc-materials only occurs under some peculiar deformation modes [65, 110] or at elevated temperatures [96]. Molecular dynamic simulation also indicated that the heavy plastic strain under high stresses is a key factor for the inducing grain growth [111]. The observed coarsening is insignificant and not expected to affect the above analysis.

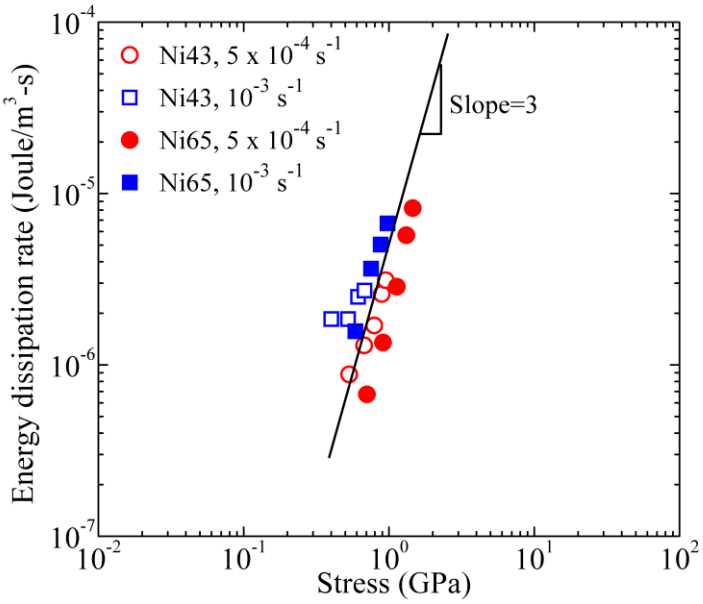

Figure 5.4 Energy dissipation rate as a function of stress for Ni65 and Ni43 in tension at different strain rates. Hollow and solid symbols represent data collected from Ni43 and Ni65, respectively.

5.4 Conclusions

Multiple interrupted unload-reload tests were conducted on nc-Ni with grain sizes of 65 and 43 nm in both compression and tension. It was found that nc-Ni exhibited hysteresis during multiple unload-reload cycles. The energy dissipation rate in each unload-reload cycle was found to be proportional to the applied stress raised to the third power and was higher in tension than in compression. The proposed grain boundary

sliding model can well describe the observed hysteresis behavior. This study demonstrates that grain boundary sliding is the dominant deformation mechanism in nc-Ni.

Chapter 6 Summary

The present research was intended to provide a better understanding of the creep behavior of nanocrystalline nickel at elevated temperatures under nanoindentation and uniaxial test, and find the correlation between the two sets of data. Efforts were also made to investigate the grain boundary sliding related mechanical hysteresis behavior of nanocrystalline nickel. Based on the experimental results, the following conclusions are made.

1. Nanoindentation creep of nc-Ni with the as-deposited grain size of 14 nm has been conducted under different peak loads and temperatures. The creep stress exponent was found generally decreased with increasing temperature and applied load. The deformation took primarily within the confined grain boundary region and grain boundary diffusion controlled the recovery process. A power-law-type equation appeared to be a convenient way to describe the nanoindentation creep behavior of nc-Ni. However, a direct comparison with the exiting literature data indicated the stress (or strain rate) level was too high to be in the power-law creep regime (i.e. controlled by dislocation climb or glide). In fact, the current nanoindentation creep data fall in the power-law breakdown regime.

2. Uniaxial and nanoindentation creep was found to have a similar stress exponent because the underpinned deformation mechanism is the same. However, the creep rate under nanoindentation is typically much faster than that under uniaxial creep. The faster creep rate was caused by the facts that the stress state under nanoindentation is more complex and severe than uniaxial condition, and the conversion factor used from hardness to stress

(i.e. the Tabor factor) is less than the typical value of 3. In fact, in the case of nc-Ni, after replacing with a proper Tabor factor, the difference between the two creeps can be brought into reasonable agreement in line with that previously observed in amorphous Se.

3. Multiple interrupted unload-reload tests have been conducted on nc-Ni with grain size of 43 and 65 nm in both tension and compression. It was found that nc-Ni exhibited hysteresis during multiple unload-reload cycles. The energy dissipation rate in each unload-reload cycle was found to be proportional to the applied stress raised to the third power and was sensitive to the stress state. We proposed a grain boundary sliding model which can well describe the observed hysteresis behavior. This study demonstrates that grain boundary sliding is the dominant mechanism in nc-Ni during unload-reload deformation mode.

Chapter 7 Suggestions for Future Research

During my study of deformation of nc-Ni, grain growth was observed after deformation at both elevated and ambient temperatures. Although ex-situ TEM experiments were conducted to examine the deformed microstructures, however, it could not reveal the exact mechanism for the observed grain growth. Therefore, a combined in-situ and ex-situ XRD and TEM experiments would be useful to shed lights on this issue. So far, there is only one report claiming grain growth during deformation of nc-material (e.g., Cu) is driven by stress not strain. It is, therefore, pertinent to perform in-situ experiment to monitor grain growth to characterize whether it is driven by stress or strain and the critical parameters that control the growth. In situ neutron scattering is a suiTable technique for this purpose. The grain growth can be determined by conducting tensile test either under strain control (hold samples at fixed displacement for a period of time) or stress control (samples are held at fixed load) condition. The strain and stress dependence of grain growth can be quantitatively evaluated by deforming samples to different strain or stress levels. The strain rate effect on the grain growth can also be evaluated by conducting uniaixal tests at different strain rates.

The grain boundary sliding model proposed in our study can well describe the mechanical hysteresis of nc-Ni. A systematic study of varying grain size is necessary to validate this model, which will provide necessary quantitative information choosing materials for the structural applications where mechanical vibration inevitably occurs. Extending the study of mechanical hysteresis behavior of nc-materials to elevated temperatures at their service conditions may also be quite interesting.

References

[1] H. Gleiter, Prog Mater Sci 33 (1989) 223.
[2] R. Birringer, Mater Sci Eng A 117 (1989) 33.
[3] H. Gleiter, Nanostr Mater 1 (1992) 1.
[4] C. Suryanarayana, Int Mater Rev 40 (1995) 41.
[5] K. Lu, Mater Sci Eng R 16 (1996) 161.
[6] J.R. Weertman, D. Farkas, K. Hemker, H. Kung, M. Mayo, R. Mitra, H.V. Swygenhoven, MRS Bulletin 24 (1999) 44.
[7] C. Suryanarayana, C.C. Koch, Hyperfine Interactions 130 (2000) 5.
[8] R.Z. Valiev, R.K. Islamgaliev, I.V. Alexandrov, Prog Mater Sci 45 (2000) 103.
[9] H. Gleiter, Acta Mater 48 (2000) 1.
[10] M. Furukawa, Z. Horita, M. Nemoto, T.G. Langdon, J Mater Sci 36 (2001) 2835.
[11] F.A. Mohamed, Y. Li, Mater Sci Eng A 298 (2001) 1.
[12] K.S. Kumar, H.V. Swygenhoven, S. Suresh, Acta Mater 51 (2003) 5743.
[13] S. Veprek, M.G.J. Veprek-Heijman, P. Karvankova, J. Prochazka, Thin Solid Films 476 (2005) 1.
[14] D. Wolf, V. Yamakov, S.R. Phillpot, A. Mukherjee, H. Gleiter, Acta Mater 53 (2005) 1.
[15] M.A. Meyers, A. Mishra, D.J. Benson, Prog Mater Sci 51 (2006) 427.
[16] G. Palumbo, S.J. Thorpe, K.T. Aust, Scripta Metall Mater 24 (1990) 1347.
[17] C.S. Pande, R.A. Masumura, R.W. Armstrong, Nanostr Mater 2 (1993) 323.
[18] T.G. Nieh, J. Wadsworth, Scripta Metall Mater 25 (1991) 955.
[19] J.K. Luo, A.J. Flewitt, S.M. Spearing, N.A. Fleck, W.I. Milne, Mater Lett 58 (2004) 2306.
[20] K. Lian, J.C. Jiang, Z.G. Ling, MICROSYSTEM TECHNOLOGIES-MICRO-AND NANOSYSTEMS-INFORMATION STORAGE AND PROCESSING SYSTEMS 13 (2007) 259.
[21] W.B. Li, J.L. Henshall, R.M. Hooper, K.E. Easterling, Acta Metall Mater 39 (1991) 3099.
[22] N. Wang, Z.R. Wang, K.T. Aust, U. Erb, Mater Sci Eng A 237 (1997) 150.
[23] G.W. Nieman, J.R. Weertman, R.W. Siegel, Scripta Metall Mater 24 (1990) 145.

[24] H. Hahn, R.S. Averback, J Amer Ceramic Soc 74 (1991) 2918.
[25] D.L. Wang, Q.P. Kong, J.P. Shui, Scripta Metall Mater 31 (1994) 47.
[26] J. Deng, D.L. Wang, Q.P. Kong, J.P. Shui, Scripta Metall Mater 32 (1995) 349.
[27] P.G. Sanders, M. Rittner, E. Kiedaisch, J.R. Weertman, H. Kung, Y.C. Lu, Nanostr Mater 9 (1997) 433.
[28] W.M. Yin, S.H. Whang, R. Mirshams, C.H. Xiao, Mater Sci Eng A 301 (2001) 18.
[29] B. Cai, Q.P. Kong, L. Lu, K. Lu, Mater Sci Eng A 286 (2000) 188.
[30] B. Cai, Q.P. Kong, P. Cui, L. Lu, K. Lu, Scripta Mater 45 (2001) 1407.
[31] Y.J. Li, W. Blum, F. Breutinger, Mater Sci Eng A 387-389 (2004) 585.
[32] Y. Ogino, Scripta Mater 43 (2000) 149.
[33] G.P. Grabovetskaya, K.V. Ivanov, Y.R. Kolobov, Ann Chim-Sci Mat 27 (2002) 89.
[34] W.M. Yin, S.H. Whang, R.A. Mirshams, Acta Mater 53 (2005) 383.
[35] R.S. Kottada, A.H. Chokshi, Scripta Mater 53 (2005) 887.
[36] V. Yamakov, D. Wolf, S.R. Phillpot, H. Gleiter, Acta Mater 50 (2002) 61.
[37] A.J. Haslam, V. Yamakov, D. Moldovan, D. Wolf, S.R. Phillpot, H. Gleiter, Acta Mater 52 (2004) 1971.
[38] A.H. Chokshi, Scripta Mater 61 (2009) 96.
[39] D.S. Tabor, The hardness of metals, Clarendon Press, Oxford, United Kingdom, 1951.
[40] J. Pomey, A. Royez, J.P. Georges, Rev Met 56 (1957) 215.
[41] T.O. Mulhearn, D. Tabor, J Inst Met 89 (1960) 7.
[42] A.G. Atkins, A. Silverio, D. Tabor, J Inst Met 94 (1966) 369.
[43] P.M. Sargent, M.F. Ashby, Mater Sci Technol 8 (1992) 594.
[44] B.L. Shen, T. Itoi, T. Yamasaki, Y. Ogino, Scripta Mater 42 (2000) 893.
[45] B. Lucas, W. Oliver, Metall Mater Trans A 30 (1999) 601.
[46] T. Chudoba, F. Richter, Surf Coat Technol 148 (2001) 191.
[47] G. Feng, A.H.W. Ngan, Scripta Mater 45 (2001) 971.
[48] F. Wang, K.W. Xu, Mater Lett 58 (2004) 2345.
[49] H. Li, A.H.W. Ngan, J Mater Res 19 (2004) 513.
[50] N. Afrin, A.H.W. Ngan, Scripta Mater 54 (2006) 7.
[51] S.P. Wen, F. Zeng, Y. Gao, F. Pan, Scripta Mater 55 (2006) 187.

[52] Z.S. Ma, S.G. Long, Y.C. Zhou, Y. Pan, Scripta Mater 59 (2008) 195.
[53] R. Mahmudi, A. Rezaee-Bazzaz, H.R. Banaie-Fard, J Alloys Comp 429 (2007) 192.
[54] R. Goodall, T.W. Clyne, Acta Mater 54 (2006) 5489.
[55] J. Weertman, Transactions of the American Institute of Mining and Metallurgical Engineerings 218 (1960) 207.
[56] W.H. Poisl, W.C. Oliver, B.D. Fabes, J Mater Res 10 (1995) 2024.
[57] C.E. Feltner, C. Laird, Acta Metall 15 (1967) 1621.
[58] C.E. Feltner, C. Laird, Acta Metall 15 (1967) 1633.
[59] S. Suresh, Fatigue of materials, Cambridge University Press, Cambridge, 1998.
[60] A.T. Winter, Philo Mag 30 (1974) 719.
[61] D. Kuhlmann-Wilsdorf, Materials Science and Engineering 39 (1979) 231.
[62] Z.S. Basinski, A.S. Korbel, S.J. Basinski, Acta Metallurgica 28 (1980) 191.
[63] B. Moser, T. Hanlon, K.S. Kumar, S. Suresh, Scripta Mater 54 (2006) 1151.
[64] S. Cheng, J. Xie, A.D. Stoica, X.L. Wang, J.A. Horton, D.W. Brown, H. Choo, P.K. Liaw, Acta Mater 57 (2009) 1272.
[65] D. Pan, T.G. Nieh, M.W. Chen, Appl Phys Lett 88 (2006) 161922.
[66] T.J. Rupert, D.S. Gianola, Y. Gan, K.J. Hemker, Science 326 (2009) 1686.
[67] Z.W. Shan, E.A. Stach, J.M.K. Wiezorek, J.A. Knapp, D.M. Follstaedt, S.X. Mao, Science 305 (2004) 654.
[68] T. Saraswati, T. Sritharan, S. Mhaisalkar, C.D. Breach, F. Wulff, Mater Sci Eng A 423 (2006) 14.
[69] C.A. Schuh, T.G. Nieh, T. Yamasaki, Scripta Mater 46 (2002) 735.
[70] J. Schiøtz, T. Vegge, F.D. Di Tolla, K.W. Jacobsen, Phys Rev B 60 (1999) 11971.
[71] M. Dao, L. Lu, R.J. Asaro, J.T.M. De Hosson, E. Ma, Acta Mater. 55 (2007) 4041.
[72] H.V. Swygenhoven, P.M. Derlet, Phys Rev B 64 (2001) 224105.
[73] D. Farkas, A. Froseth, H.V. Swygenhoven, Scripta Mater 55 (2006) 695.
[74] M.D. Uchic, D.M. Dimiduk, J.N. Florando, W.D. Nix, Science 305 (2004) 986.
[75] W.C. Oliver, G.M. Pharr, J Mater Res 7 (1992) 1564.
[76] W.C. Oliver, G.M. Pharra, J Mater Res 19 (2004) 3.
[77] www.hysitron.com.

[78] C.A. Schuh, A.C. Lund, T.G. Nieh, Acta Mater 52 (2004) 5879.
[79] www.microstartech.com.
[80] J. Alkorta, J.M. Martínez-Esnaola, J. Gil Sevillano, Acta Mater 56 (2008) 884.
[81] T. Neeraj, D.H. Hou, G.S. Daehn, M.J. Mills, Acta Mater 48 (2000) 1225.
[82] Y.J. Li, J. Mueller, H.W. Hoppel, M. Goken, W. Blum, Acta Mater 55 (2007) 5708.
[83] I. Brooks, P. Lin, G. Palumbo, G.D. Hibbard, U. Erb, Mater Sci Eng A 491 (2008) 412.
[84] A.R. Wazzan, J Appl Phys 36 (1965) 3596.
[85] K. Monma, H. Suto, H. Oikawa, J Jpn Inst Met 28 (1964) 188.
[86] R.J. Asaro, S. Suresh, Acta Mater 53 (2005) 3369.
[87] C.D. Gu, J.S. Lian, Q. Jiang, W.T. Zheng, J Phys D: Appl Phys 40 (2007) 7440.
[88] D. Caillard, J.L. Martin, Thermally activated mechanisms in crystal plasticity, Pergamon, Amsterdam, 2003.
[89] N. Wang, Z.R. Wang, K.T. Aust, U. Erb, Acta Mater 45 (1997) 1655.
[90] R. Klemm, E. Thiele, C. Holste, J. Eckert, N. Schell, Scripta Mater 46 (2002) 685.
[91] M. Chauhan, F.A. Mohamed, Mater Sci Eng 427 (2006) 7.
[92] K. Zhang, J.R. Weertman, J.A. Eastman, Appl Phys Lett 87 (2005) 061921.
[93] S. Brandstetter, K. Zhang, A. Escuadro, J.R. Weertman, H.V. Swygenhoven, Scripta Mater 58 (2008) 61.
[94] V.N. Chuvil'deev, T.G. Nieh, M.Y. Gryaznov, A.N. Sysoev, V.I. Kopylov, Scripta Mater 50 (2004) 861.
[95] O.D. Sherby, J. Wadsworth, Prog Mater Sci 33 (1989) 169.
[96] S.X. McFadden, R.S. Mishra, R.Z. Valiev, A.P. Zhilyaev, A.K. Mukherjee, Nature 398 (1999) 684.
[97] J.R. Spingarn, B.E. Jacobson, W.D. Nix, Thin Solid Films 45 (1977) 507.
[98] G.M. Pharr, Scripta Metall 15 (1981) 713.
[99] T.R.G. Kutty, K. Ravi, C. Ganguly, J Nucl Mater 265 (1999) 91.
[100] D.R. Lesuer, J. Wadsworth, T.G. Nieh, Ceram Int 22 (1996) 381.
[101] J. Moteff, R. Bhargava, W. McCullough, Metall Mater Trans A 6 (1975) 1101.

[102] J.F. Ziegler, J.P. Biersach, U. Littmark, U. The Stopping and Range of Ions in Solids, Stopping and
Range of Ions in Matter, (Pergamon, New York, 1985).
[103] G.C. Wood, I.G. Wright, J.M. Ferguson, Corros Sci 5 (1965) 645.
[104] A.C. Lund, C.A. Schuh, Acta Mater 53 (2005) 3193.
[105] A.C. Lund, T.G. Nieh, C.A. Schuh, Phys Rev B 69 (2004) 012101.
[106] B.E. Schuster, Q. Wei, H. Zhang, K.T. Ramesh, Appl Phys Lett 88 (2006) 103112.
[107] J.H. Schneibel, P.M. Hazzledine, Acta Metall. 30 (1982) 1223.
[108] B.S. Bokstein, H.D. Bröse, L.I. Trusov, T.P. Khvostantseva, Nanostruct Mater 6 (1995) 873.
[109] S.V. Divinski, G. Reglitz, G. Wilde, Acta Mater 58 (2010) 386.
[110] X.Z. Liao, A.R. Kilmametov, R.Z. Valiev, H.S. Gao, X.D. Li, A.K. Mukherjee, J.F. Bingert, Y.T. Zhu, Appl Phys Lett 88 (2006) 021909.
[111] J. Schiøtz, Mater Sci Eng A 375-377 (2004) 975.

VITA

Changli, Wang was born in China in 1976. She was raised in Baoqing, China. After graduated from Baoqing High School, Baoqing, China in 1995, she attended Harbin Institute of Technology and completed her undergraduate study in the School of Materials Science and Engineering in 1999 and master study in 2001 in the same department. She worked as a research assistant at The Hong Kong Polytechnic University, Hong Kong for two and a half years before coming to The University of Tennessee, Knoxville in January 2006, where she started to pursue a doctorate in Materials Science and Engineering. She received a Ph.D degree under the guidance of Professor T. G. Nieh in 2010.